# Topographic Influences on Wind-Driven, Stratified Flow in a $\beta$-Plane Channel: An Idealized Model for the Antarctic Circumpolar Current

A. M. TREGUIER

*IFREMER, Brest, France*

J. C. MCWILLIAMS

*National Center for Atmospheric Research, Boulder, Colorado*

(Manuscript received 15 May 1989, in final form 21 August 1989)

ABSTRACT

Topographic influences are examined in an eddy-resolving model of oceanic channel flow forced by steady zonal winds. With small explicit lateral friction, transient eddies generated by the baroclinic instability of the mean flow transfer momentum downward to the bottom layer. In the flat-bottom case, bottom friction is the only efficient sink of eastward momentum. When bottom topography is present, the topographic form stress can replace the bottom friction sink in the momentum budget, and a large decrease of the zonal transport results. Large scale topography (of the scale of the forcing) provides the largest form stress. Topographic effects decay with height as suggested by the Prandlt scaling, and therefore only topographic scales larger than the Rossby radius can affect the whole water column. In that case, the interfaces are deformed by standing eddies on topographic length scales, and standing eddies replace transient eddies in transferring momentum downward. The bottom-layer mean streamfunction tends to be correlated with the topography as in inviscid solutions. Because of this, only a small part of the flow (the larger scales) contributes to the domain-averaged momentum sink. On smaller scales, the topographic form stress is anticorrelated with the Reynolds stress and has no net effect on the transport. The energy level of the transients is less affected by the topography than is the mean energy. With topography, the space scale of the transients decreases and their time scale increases, and the ratio of potential and kinetic energies is higher.

## 1. Introduction

The problem of the momentum balance of the Antarctic Circumpolar Current (ACC) has motivated many numerical studies of oceanic channel flows. In the early coarse-resolution models (e.g., Gill and Bryan 1971) the momentum input by the wind was balanced by lateral mixing. When the first quasi-geostrophic eddy-resolving models were run 10 years ago, it appeared that in the absence of large lateral friction the flow was unstable and meandering, and therefore more realistic. On the other hand, flat-bottom models gave zonal transports one order of magnitude too large (1000 Sv instead of an order of 100 Sv; Sv $\equiv 10^6$ m$^3$ s$^{-1}$) with reasonable values of the wind stress and bottom friction coefficient. Following the early suggestion of Munk and Palmen (1951), McWilliams et al. (1978) showed that including a representation of the Drake Passage (a strait partially obstructed by bottom topography) could reduce the transport to reasonable values. In that case, the main eastward momentum sink in the bottom layer was no longer the bottom friction drag but rather the topographic form stress (also called topographic drag) resulting from different pressure forces on each side of the topography. This early study however left many questions unanswered. For example, how high must the topography be to be an efficient momentum sink? Is the transport very dependent on the shape of the topography? Does the horizontal scale of the topography matter?

Some of these questions have been addressed in a recent paper by Wolff and Olbers (1989). They have considered different topographic shapes, seamounts or meridional ridges partially or totally obstructing the channel. Their results show that, indeed, the transport is highly dependent on the position and shape of the topography.

The present paper compares quasi-geostrophic solutions with isolated topographies similar to those of Wolff and Olbers (1989) and solutions with randomly distributed topographies. Using a broader class of topographic fields allows us to point out new features of the momentum balance, for example, an anticorrelation between the Reynolds stress and the topographic form stress in the bottom layer. An examination of the statistics of the standing eddies, especially their vertical

*Corresponding author address:* Dr. A. M. Treguier, DERO/EO, IFREMER, BP. 70, 29263 Plouzane, France.

penetration and correlation with the topographic field, is necessary in order to understand the momentum balance in those cases. By using random topographies with different wavenumber spectra, we demonstrate that topography with large spatial scales has the largest effect on the momentum balance of the current in the context of our model. Finally, a calculation of the energy balance shows the influence of topography on baroclinic and barotropic instability processes.

The next two sections of the paper introduce the model and review basic features of the dynamics already pointed out by previous authors. Section 4 describes topographic influences on the statistics of the transients and the mean flow, as well as the correlation of the mean streamfunction and vorticity field with topography. The implications of such correlations for the momentum and energy balances are discussed in section 5. Section 6 deals with the variations of zonal transport and topographic form stress as a function of the topographic height and spatial scale. Finally, the spatial structure of the topographic form stress is examined in detail in section 7, with implications as to its measureability.

## 2. Model equations and parameters

McWilliams and Chow (1981, hereafter MC81) performed a thorough analysis of flow driven by a steady eastward wind stress in a flat-bottom channel. Their model is used here, the only difference being the introduction of bottom topography. The quasi-geostrophic vorticity equation on a $\beta$-plane is for layer $k$

$$\frac{\partial q_k}{\partial t} + J(\psi_k, q_k) = -\nu\nabla^6\psi_k + \delta_{1,k}\frac{\text{curl}(\tau)}{\rho H_1} - \delta_{n,k}\epsilon\nabla^2\psi_k, \quad (1)$$

where $\psi_k$ is the streamfunction and $q_k$ is the potential vorticity in layer $k$

$$q_k = \nabla^2\psi_k + \beta y + \delta_{n,k}\tilde{h} + \frac{f_0^2}{g'_{k-1/2}H_k}(\psi_{k-1} - \psi_k) - \frac{f_0^2}{g'_{k+1/2}H_k}(\psi_k - \psi_{k+1}).$$

This expression is valid in all layers with the convention that the reduced gravity $g'$ is infinite above the top layer and below the bottom layer $k = n$. The topography is $\tilde{h} = f_0 h/H_n$, $h$ being the topographic elevation and $H_n$ the bottom-layer depth. The energy source for the flow is the zonal wind stress $\tau$ which accelerates the top layer, and the main energy sink is the bottom friction with characteristic decay time $\epsilon^{-1}$ in the bottom layer. Biharmonic friction with coefficient $\nu$ is added as a subgrid-scale parameterization and provides a secondary energy sink.

The boundary conditions on the north and south channel walls are

$$\frac{\partial\psi_k}{\partial x} = 0, \quad \nabla^2\psi_k = 0, \quad \nabla^4\psi_k = 0, \quad \text{for} \quad y = y_N \quad \text{and} \quad y = y_S.$$

The momentum equation integrated along the south boundary and the mass conservation are used as auxiliary conditions to calculate the streamfunction on the walls (McWilliams 1977). The equations are solved using classical finite-difference methods (Holland 1978 MC81).

Two sets of parameters have been used (Table 1), with many different topographic fields for each (Table 2). Using different parameters prevents quantitative comparisons between the two sets of experiments, but

TABLE 1. Parameters for the two sets of experiments.

| | | | 4L experiments | 3L experiments |
|---|---|---|---|---|
| Horizontal resolution | Channel length | $L_x$ | 1875 km | 2250 km |
| | Channel width | $L_y$ | 1250 km | 1500 km |
| | Gridpoints | | 144 × 96 | 144 × 96 |
| Vertical resolution | Number of layers | $N$ | 4 | 3 |
| | Layer depths | $H_1$ | 500 m | 500 m |
| | | $H_2$ | 1000 m | 1000 m |
| | | $H_3$ | 1000 m | 3500 m |
| | | $H_4$ | 2500 m | |
| | Rossby radii | $R_1$ | 36 km | 37 km |
| | | $R_2$ | 17.5 km | 17.6 km |
| | | $R_3$ | 14 km | |
| Coriolis parameter | | $f_0$ | $8.35 \times 10^{-5}$ s$^{-1}$ | $-1.1 \times 10^{-4}$ s$^{-1}$ |
| | | $\beta$ | $1.9 \times 10^{-11}$ m$^{-1}$ s$^{-1}$ | $1.4 \times 10^{-11}$ m$^{-1}$ s$^{-1}$ |
| Forcing | shape | | $\sin(y)$ | $\sin^2(y)$ |
| | maximum $\tau_x/\rho$ | $\tau_0$ | $1 \times 10^{-4}$ m$^2$ s$^{-2}$ | $1 \times 10^{-4}$ m$^2$ s$^{-2}$ |
| Friction | Bottom friction | $\epsilon$ | $10^{-7}$ s$^{-1}$ | $10^{-7}$ s$^{-1}$ |
| | Biharmonic friction | $\nu$ | $1.8 \times 10^9$ m$^4$ s$^{-1}$ | $3.8 \times 10^9$ m$^4$ s$^{-1}$ |

TABLE 2. Topography used in the experiments. Except for case 4L5, the spectrum for randomly generated topography is truncated at a minimum wavelength of 52 km. $h$ is the rms height and $L_t$ the inverse of the average wavenumber.

| Case | $h$ (m) | $L_t$ (km) | Comments |
|---|---|---|---|
| 4L0 | | | no topography. |
| 4L1 | 100 | 109 | $K^{-2}$ spectrum, maximum wavelength 208 km. |
| 4L2 | 400 | 109 | $K^{-2}$ spectrum, maximum wavelength 208 km. |
| 4L3 | 100 | 164 | $K^{-2}$ spectrum, maximum wavelength 417 km. |
| 4L4 | 400 | 164 | $K^{-2}$ spectrum, maximum wavelength 417 km. |
| 4L5 | 297 | 164 | $K^{-2}$ spectrum, maximum wavelength 417 km. |
| 4L6 | 297 | 280 | $K^{-2}$ spectrum, maximum wavelength 417 km, minimum wavelength 208 km. |
| 4L7 | 200 | 231 | $(K_0^2 + K^2)^{-1}$ spectrum, $2\pi/K_0$ = 417 km. |
| 4L8 | 400 | 231 | $(K_0^2 + K^2)^{-1}$ spectrum, $2\pi/K_0$ = 417 km. |
| 4L9 | 200 | 455 | $K^{-2}$ spectrum, maximum wavelength 1250 km. |
| 3L0 | | | no topography. |
| 3L1 | 16.4 | 172 | Centered seamount. Radius = 120 km, height = 200 m. |
| 3L2 | 24.6 | 172 | Centered seamount. Radius = 120 km, height = 300 m. |
| 3L3 | 41 | 172 | Centered seamount. Radius = 120 km, height = 500 m. |
| 3L4 | 82 | 172 | Centered seamount. Radius = 120 km, height = 1000 m. |
| 3L5 | 64.6 | 145 | Seamount as 3L3 with added noise: $h$ = 50 m, $K^{-2}$ spectrum, maximum wavelength 250 km. |
| 3L6 | 62.3 | 180 | Seamount as 3L3 with added noise: $h$ = 50 m, $K^{-2}$ spectrum, maximum wavelength 500 km. |
| 3L7 | 25.9 | 954 | Meridional ridge. Zonal scale = 120 km, height = 100 m. |
| 3L8 | 51.7 | 954 | Meridional ridge. Zonal scale = 120 km, height = 200 m. |
| 3L9 | 129.3 | 954 | Meridional ridge. Zonal scale = 120 km, height = 500 m. |

it gives more confidence in the generality of the qualitative behavior observed in both cases. In the first set of experiments, the emphasis is on good spatial resolution, with four layers vertically and a horizontal grid scale of 13 km. The domain is relatively small (1875 × 1250 km), and the Coriolis parameter $f_0$ and $\beta$ effect are typical of midlatitudes. These parameters are chosen to study the effect of random small and mesoscale topography, where a good vertical and horizontal resolution is essential since topography induces a cascade of energy to small horizontal scales and important bottom-trapped motions. The second set of experiments explores the effect of large-scale, deterministic topography. The channel is larger, the resolution is lower (Table 1), and $f_0$ and $\beta$ are typical of the Southern Ocean to allow comparison with the simulations of Wolff and Olbers (1989) and MC81. Note that, like previous authors, we have kept a stratification typical of midlatitudes (first Rossby radius $R_1$ = 36 km) instead of the Southern Ocean ($R_1$ = 20 to 25 km at 50°S) because a realistic small Rossby radius would require a very high resolution. For the first set of parameters (solutions whose label begins with 4L) the wind stress is proportional to $\tau_0 \sin y$. For the second set (labeled 3L), a $\sin^2 y$ shape has been used in order to obtain a more concentrated jet despite the broader channel and minimize the influence of the channel boundaries. The two forcing shapes produce qualitatively similar flows.

Random topography is generated from a horizontally isotropic spectrum. The topographic height is set to a constant along the channel walls (similar to the boundary condition for the streamfunction) to avoid the formation of a boundary layer in the relative vorticity field (Treguier 1989). In most cases the spectrum is a band-limited $K^{-2}$ spectrum between wavenumbers $K_{\min}$ and $K_{\max}$. When $K_{\max}$ corresponds to the gridscale, the topographically induced cascade of energy towards small scales is such that biharmonic friction can become the main energy sink. Since biharmonic friction is a subgridscale parameterization, it is reasonable to simulate only flows in which its effect remains small compared to bottom friction, and therefore the minimum topographic wavelength ($2\pi/K_{\max}$ = 52 km) is chosen larger than the model gridscale. The other limit of the spectrum (the maximum wavelength) is varied to study the effect of different topographic spatial scales (Table 2). Besides the $K^{-2}$ spectrum, a spectrum proportional to $(K_0^2 + K^2)^{-1}$ has been used in two cases, 4L7 and 4L8.

The study of isolated topographies concentrates on two simple shapes: an isolated seamount

$$h(x, y) = h_m e^{-(x^2+y^2)/r^2}, \tag{2}$$

with radius $r$ = 120 km centered in the middle of the channel, or a ridge of same shape and width in $x$ but independent of $y$. Different maximum heights $h_m$ ranging from 100 to 1000 m have been used. The combined effects of random and isolated topographies have been studied in cases 3L5 and 3L6.

## 3. Channel flows with and without topography: Review

### *a. Dynamics of flat-bottom solutions*

In a steady-state solution with small lateral friction, energy must be transferred from the surface layer downward to the bottom layer where all the dissipation takes place. Only transients can generate such a time-averaged downward flux in the quasi-geostrophic system with zero vertical viscosity. Therefore, the flow in the upper layer accelerates until it becomes baroclinically unstable, and equilibrium is reached when the downward transfer of energy by transient eddies is equal to the input by the wind. Barotropic instability plays

a small part away from lateral boundaries when the meridional scale of the forcing is large.

Figure 1a shows a classical energy diagram for our flat-bottom case 4L0, similar to the one displayed in Fig. 8 of MC81 for their case I. The main energy pathway is from mean kinetic energy to potential energy, and then to transient potential and kinetic energies, reflecting the baroclinic instability mechanism. Note that eddy kinetic energy is converted into mean kinetic energy by the Reynolds stress divergence which concentrates and intensifies the jet (an opposite transfer would indicate barotropic instability). MC81 (Fig. 24) found that the shape of the Reynolds stress divergence is also a property of the linearly unstable modes of the mean jet. Although the basic dynamics of case 4L0, 3L0 and case I of MC81 are similar, the energy level is larger in 4L0 because $\beta$ is larger and therefore the flow is less baroclinically unstable.

Transport is very large in flat-bottom solutions (1859 Sv for 4L0 and 1250 Sv for 3L0) since the mean flow is zonal and almost barotropic. In solution 4L0, 97% of the mean kinetic energy and 80% of the transient kinetic energy is barotropic. The barotropic mode is efficiently forced by the wind in the channel geometry, because the barotropic mean streamfunction and the wind-stress curl have similar shapes. This contrasts with closed basin geometries in which the baroclinic modes receive most of the forcing energy. In a classical double-gyre solution in a rectangular basin (e.g., Holland 1978) the barotropic recirculation is narrow and concentrated near the central latitude of the free jet, whereas the baroclinic streamfunction has a structure similar to the cosine shape of the wind-stress curl, allowing a large baroclinic forcing.

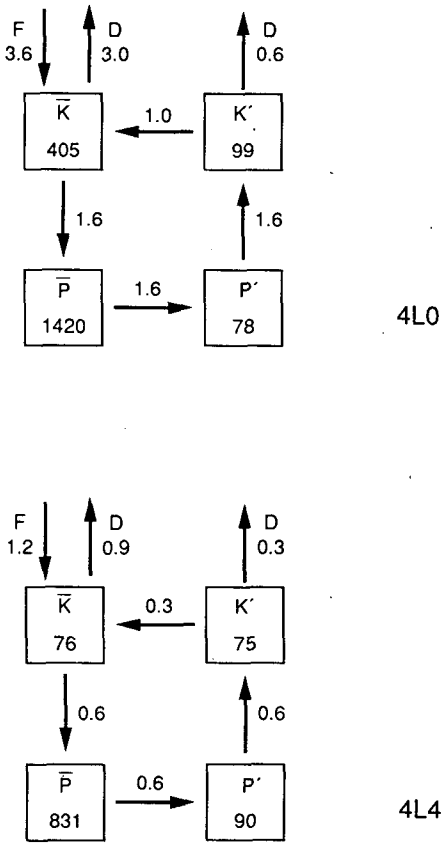


FIG. 1. Global energy budgets integrated over the four layers for flat-bottom solution 4L0 and topographic solution 4L4. $K$ is the kinetic energy, $P$ the potential energy, $F$ the forcing, $D$ the total dissipation, and the other arrows are nonlinear transfers. Units are $m^3\ s^{-2}$ for energies and $10^{-5}\ m^3\ s^{-3}$ for energy transfers.

### b. *Dynamics of a solution with topography*

Case 4L4 is identical to 4L0, but with a mesoscale random topography with rms height 400 m. The effect of topography is much greater on the mean flow than on the transients, as shown by the energy diagrams (Fig. 1b). The transient kinetic energy $K'$ is decreased by 25% between cases 4L0 and 4L4, but the mean kinetic energy $\bar{K}$ is 5 times smaller. In the presence of topography the time–mean flow is no longer zonal, but exhibits meanders and standing eddies even in the upper layers. This greatly reduces the forcing efficiency since the zonal forcing is uncorrelated with the standing eddies by definition. The zonal transport is reduced from 1859 Sv to only 275 Sv. The flow is also less barotropic: the barotropic mode in 4L4 accounts for 82% of the mean kinetic energy and 68% of the transient kinetic energy.

The zonal momentum balance has often been used to understand the effect of topography on the transport (McWilliams et al. 1978; Wolff and Olbers 1989). Representing the zonal average by brackets $\langle\ \rangle$, the time-average by an overbar and the time fluctuations by a prime, the zonal momentum balance in layer $k$ is

$$\frac{\partial\langle\overline{u_k}\rangle}{\partial t} = 0 = \delta_{1,k}F + R_k + H_k^{-1}(D_{k-1/2} - D_{k+1/2}) + \delta_{n,k}(B + T). \quad (3)$$

The biharmonic friction is found to be negligible in all our momentum budgets and has been omitted here for simplicity. The Reynolds stress divergence $R_k$ and the interfacial form stress $D_{k+1/2}$ are

$$R_k = -\frac{\partial\langle\overline{u_k'v_k'}\rangle}{\partial y} \quad (4)$$

$$D_{k+1/2} = \frac{f_0^2}{g'_{k+1/2}}\left\langle\overline{\psi_k\frac{\partial}{\partial x}\psi_{k+1}}\right\rangle. \quad (5)$$

The wind stress forcing $F = \langle\bar{\tau}\rangle/\rho H_1$ appears in the upper layer and the bottom friction drag $B = -\epsilon\langle\overline{u_n}\rangle$ in the lower layer $n$. Topography influences

the momentum balance through the topographic form stress $T$

$$T = \langle \overline{v_n} \tilde{h} \rangle = -\left\langle \overline{\psi_n} \frac{\partial \tilde{h}}{\partial x} \right\rangle \quad (6)$$

Note that we prefer the term "form stress" instead of "form drag" since $T$ does not necessarily resist the mean flow (e.g., does not always act as a drag).

By summing (3) over the layers and latitudes one obtains a simple balance between the wind stress, bottom friction and topographic form stress:

$$\epsilon \overline{M_n} = \bar{F} + \bar{T}, \quad (7)$$

where $\overline{M_n}$ is the transport in the lower layer, $\bar{F}$ is the wind stress forcing and $\bar{T}$ the topographic form stress integrated over the channel width $L$ and the depth. For the flat-bottom case 4L0 with a sinusoidal forcing,

$$\overline{M_n} = \frac{\bar{F}}{\epsilon} = \frac{2L\tau_0}{\pi\epsilon} = 796 \times 10^6 \text{ m}^3 \text{ s}^{-1}. \quad (8)$$

The total transport, however, cannot be derived from a simple equation (it would be $2 \times 796$ Sv in a purely barotropic solution instead of the actual 1859 Sv in 4L0). Topographic solutions like 4L4 are different from flat-bottom solutions because the topographic form stress $\bar{T}$ can balance the wind stress ($\bar{T}/\bar{F} = -0.95$ in 4L4), and the bottom friction drag can be small, resulting in a reduced lower layer transport (47 Sv). In case 4L4 83% of the total transport (228 Sv) occur in the upper 2500 m, compared with only 57% in the flat-bottom case.

An important conclusion, stressed by McWilliams et al. (1978), is that topography makes the eddy-resolving model a much more acceptable representation of the statistics of the Antarctic Circumpolar Current. With reasonable values for the wind stress and friction coefficients, one can obtain acceptable values for the transport and kinetic energies. The upper-level eddy kinetic energy is larger than the mean (instead of being smaller as in the flat-bottom case), and the amplitude of the barotropic mode is reduced. Therefore, a more extensive study of topographic influence in such a model seems warranted.

## 4. Statistics of the solutions with topography

In the following, the transients and steady flow are discussed separately because topography affects them differently. The steady component is determined by averaging over 5 to 12 years of simulation. A few tests have shown that averaging over longer periods does not change the results.

### *a. Transient flow*

Topography generates a cascade of energy towards small horizontal scales in quasi-geotrophic turbulence (Rhines 1977; Treguier and Hua 1988, hereafter TH88). In our solutions with topography the horizontal scale of the transients is smaller by two measures. First, the typical diameter of the energetic transient eddies tends to decrease slightly, especially with the large scale random topographies. In those cases the mean flow has a complicated spatial structure at all depths (an example is shown in Fig. 3) and the transient eddies produced by baroclinic instability have complex shapes, whereas in the flat-bottom case the eddies are larger and almost symmetric about the jet axis. Second, when small scale topography is present the amount of eddy enstrophy in the lower layer increases. The ratio of the transient kinetic energy $K'_4$ and enstrophy $Z'_4$ gives a length scale of 50 km for the flat-bottom case 4L0 and 25 km for case 4L4. This decrease is due to small scale structure superimposed on the dominant transient eddies in the lower layer. It does not happen when the topography exists only at large scales (3L experiments with isolated topographies).

Topography also modifies the time scale of the transients. In the flat-bottom solutions, kinetic energy frequency spectra are red near the walls, but in the center of the channel they are dominated by resonant peaks associated with the largest scale linear Rossby waves for periods longer than 10 days (MC81, Fig. 17). The influence of topography is greatest in that central region: the resonant peaks at periods of 10 to 50 days become smaller or disappear entirely, and the kinetic energy spectra become almost as steep as $\omega^{-2}$. Besides the decrease of energy at periods of 10 to 100 days, in some cases there is an increase of kinetic energy at periods larger than 100 days. Those modifications of the spectra are reflected by an increase of the average time scale near the center of the channel. The inverse of the mean frequency $\bar{f} = \sum K(f) f df / \sum K(f) df$, where $K$ is the kinetic energy, gives an estimate of the time scale. In the lower layer this time scale increases from 25 days in the flat-bottom case 4L0 to 74 days in 4L4. The effect is larger for the highest topographies, but our results do not show any net dependency on the topographic shape (isolated or random) or horizontal scale. The reduced amplitude of the spectral peaks is due to the modification of the dispersion relation of barotropic Rossby waves in the presence of topography. A similar effect appears in TH88, but the average time scales were less altered probably because they were constrained by the transient wind forcing.

In TH88 topography was found to induce a surface intensification of the transients. The effect was not very large (a factor of two) but the surface intensification exhibited a clear dependency on the topographic rms slope. In the present study there is also about a factor of two between the less and the more surface-intensified cases. The larger surface intensification corresponds to a larger baroclinicity of the flow and an enhanced transient potential energy (for example, the ratio $P'/K'$ increases between cases 4L0 and 4L4, Fig. 1b). However,

there are important differences between the vertical structure of the present solutions and TH88. First, the domain-averaged surface intensification of the kinetic energy (between 2.5 and 5) is smaller than the values between 6 and 12 found by TH88, probably because the nonlinear transfer of energy from the baroclinic to the barotropic mode due to baroclinic instability is larger in the channel model. Second, in our solutions there is no simple dependency of the surface intensification on the rms height or slope of the topography, reflecting the different dynamics of transient motions directly forced by wind fluctuations (in TH88) and transient motions generated from the baroclinic instability of a mean zonal flow (in the present model).

*b. Time-mean flow*

In the presence of topography the mean flow is no longer purely zonal and standing eddies are present. Quantities associated with the zonal mean flow are noted by brackets and quantities associated with the standing eddies are noted by an asterisk. Two characteristics of the standing eddies are described: their vertical structure and their correlation with the topographic field.

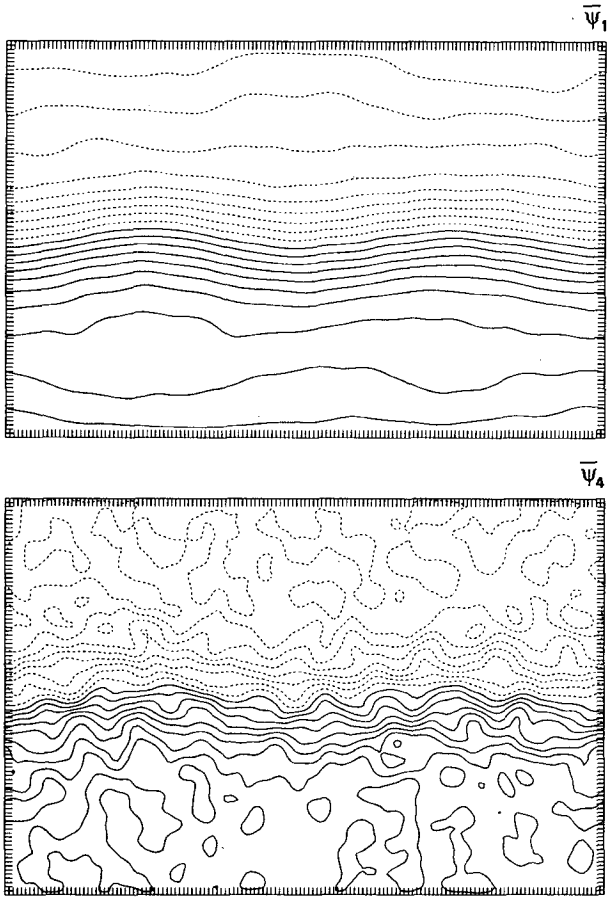


FIG. 2. Time-mean streamfunction in the upper and lower layer for solution 4L2 with small scale topography. Contours intervals are $2 \times 10^4$ m$^2$ s$^{-1}$ for $\bar{\psi}_1$ and $10^4$ m$^2$ s$^{-1}$ for $\bar{\psi}_4$.

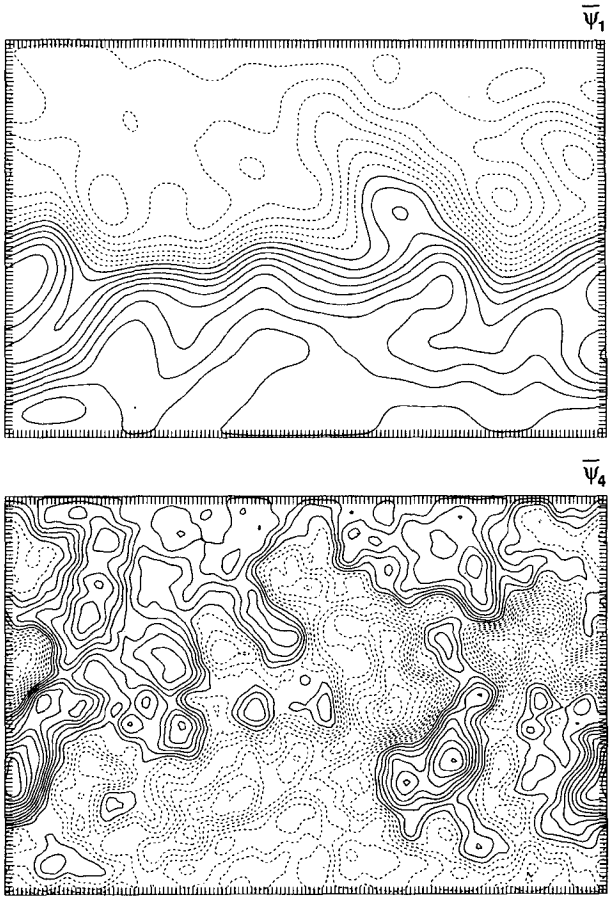


FIG. 3. As in Fig. 2 but for solution 4L8 with large scale topography. Contours intervals are $6 \times 10^4$ m$^2$ s$^{-1}$ for $\bar{\psi}_1$ and $2 \times 10^4$ m$^2$ s$^{-1}$ for $\bar{\psi}_4$.

1) VERTICAL STRUCTURE OF THE TIME-MEAN FLOW

For the cases with small scale topography (4L1 and 4L2), the effect of topography is concentrated in the bottom layer as shown in Fig. 2. Standing eddies appear clearly in the lower layer whereas the mean flow in the upper layer is essentially zonal, as in the flat-bottom case. The kinetic energy $\overline{K_*}$ of the standing eddies decreases by a factor 5 between the bottom layer and the top layer.

The effect of topography penetrates into the upper layers when there is a permanent deformation of the interfaces at least partly reproducing the topographic shape. In that case, the interfacial form stress in the upper layers plays the same part as the topographic form stress in the bottom layer. This happens in case 4L8 with a larger scale topography (Fig. 3). The kinetic energy $\overline{K_*}$ of the standing eddies is the same in the top

and bottom layers for that case. In all of the 3-layer solutions, the interfacial form stress is more efficient than the topographic form stress and the standing eddies are surface-intensified ($\overline{K_*}$ can be as much as 6 times larger in the upper layer than in the lower layer).

This vertical structure merely reflects the familiar behavior of stratified fluids: motions associated with topographic scales larger than the Rossby radius affect the whole water column whereas motions with smaller horizontal scales remain trapped at the bottom. One may expect topographic effects to decay with height with the Prandlt $e$-folding scale

$$h_e = f_0 L_t / \mathcal{N}, \tag{9}$$

where $L_t$ is the topographic horizontal scale and $\mathcal{N}$ is the Brunt-Väisälä frequency. For example, $h_e$ is the $e$-folding scale for the vertical structure of linear waves on a sloping bottom (Rhines 1970).

Our simulations qualitatively agree with (9). Table 3 shows the percentage of mean kinetic energy in the standing eddies $S = \overline{K_*}/(\overline{K_*} + \langle \bar{K} \rangle)$ for 4-layer experiments with different topographic horizontal scales (qualified by small, medium, large and largest) and different rms heights. Clearly $S$ depends on both parameters. Also shown is $S_0$, equal to $S(z)$, normalized by its bottom value to provide an estimate of the vertical penetration of topographic effects. Here $S_0$ does not depend much on the topographic height and decays more quickly with height for smaller scale topography as expected from a Prandlt scaling. In order to perform a quantitative test of (9), one may estimate $\mathcal{N}$ in the layer model by assuming that the density jump $g'_{k+1/2}$ is spread over the height $(H_k + H_{k+1})/2$, and take for the topographic scale $L_t$ the inverse of the average topographic wavenumber given in Table 2. For the small scale topography one obtains $h_e = 1000$ m and a decay from 1.0 to 0.17 between layers 4 and 3, which is in good agreement with the vertical structure of $S_0$. For the "mesoscale" and "large scale" topographies $L_t$ is similar, and $h_e \approx 2500$ m. The corresponding decay from 1.0 to 0.3 between layers 4 and 3 is much quicker than the actual decay of $S_0$ in those cases. For a better agreement one could choose a measure of $L_t$ giving more weight to the larger topographic scales. For instance, the largest topographic scale $L_t = K_{\min}^{-1}$ gives $h_e \approx 11\,000$ m for the "large" and "largest scale" topographies, corresponding to a decay from 1.0 to 0.86 beteween layers 4 and 3, close to the values of Table 3. For the isolated topographies, $S_0$ is almost uniform with depth, and one could take for $L_t$ the diameter of the seamount.

Table 3 demonstrates that the penetration of topographic effects qualitatively obeys a Prandlt scaling in our solutions. However, no quantitative estimate of a penetration scale can be made a priori because there is some arbitrariness in the definition of $L_t$ when the topography has a broad band spectrum. Moreover, there is a small nonlinear dependency on the topographic rms height (Table 3), and other parameters probably play a part ($\beta$ for example should inhibit vertical penetration).

### 2) FLOW–TOPOGRAPHY CORRELATIONS

Mean currents correlated with the topography tend to develop in turbulent flows, as shown for example by the numerical simulations of Bretherton and Haidvogel (1976). In their barotropic model of decaying turbulence, the standing eddies adjusted in many cases to an approximately linear relationship between the mean streamfunction and the potential vorticity, and a zonal westward flow developed in the presence of $\beta$:

$$\overline{\psi_*} = \mu^{-2}(\nabla^2 \overline{\psi_*} + \tilde{h}) \,,$$
$$\langle \bar{\psi} \rangle = -Uy = (\mu^{-2}\beta)y. \tag{10}$$

All steady solutions in an inviscid quasi-geostrophic model satisfy

$$\bar{\psi} = \mathcal{F}(\nabla^2 \bar{\psi} + \tilde{h} + \beta y), \tag{11}$$

TABLE 3. Vertical penetration of topographic influence.

| | Case | | | | | | |
|---|---|---|---|---|---|---|---|
| | 4L1 | 4L2 | 4L3 | 4L4 | 4L7 | 4L8 | 4L9 |
| Topographic scale | small | | medium | | large | | largest |
| Rms height (m) | 100 | 400 | 100 | 400 | 200 | 400 | 200 |
| Layer | Percentage of mean nonzonal kinetic energy $S$ | | | | | | |
| $K = 1$ | 0 | 4 | 1 | 32 | 59 | 57 | 70 |
| $K = 2$ | 0 | 4 | 1 | 39 | 68 | 63 | 74 |
| $K = 3$ | 0 | 10 | 2 | 67 | 82 | 88 | 76 |
| $K = 4$ | 2 | 43 | 5 | 92 | 90 | 98 | 84 |
| Layer | Percentage normalized by bottom value $S_0$ | | | | | | |
| $K = 1$ | .05 | .09 | .29 | .35 | .66 | .58 | .83 |
| $K = 2$ | .04 | .09 | .23 | .43 | .75 | .65 | .88 |
| $K = 3$ | .15 | .24 | .39 | .73 | .91 | .90 | .91 |
| $K = 4$ | 1.0 | 1.0 | 1.0 | 1.0 | 1.0 | 1.0 | 1.0 |

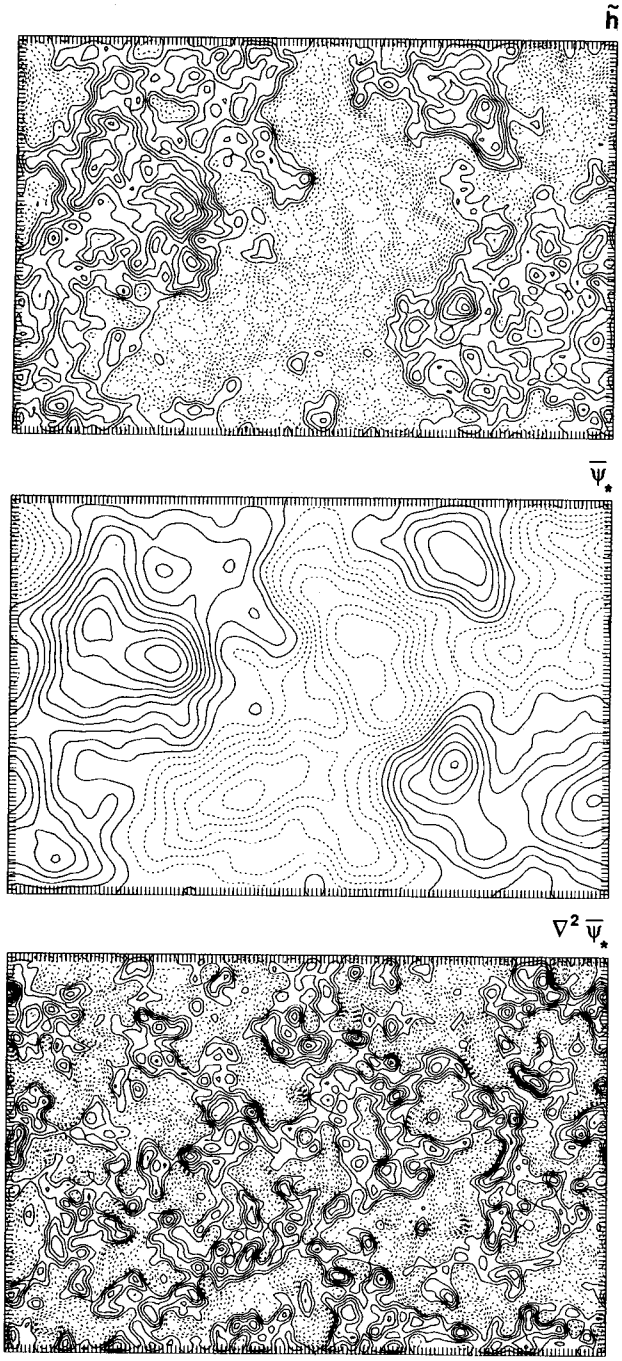


FIG. 4. Correlation of the flow with topography in the bottom layer for case 4L9. (a) Topographic field $\tilde{h}$, contour intervals is $2 \times 10^{-4}$ s$^{-1}$. (b) Nonzonal streamfunction $\overline{\psi}_*$, contour interval is 3000 m$^2$ s$^{-1}$. (c) Relative vorticity, contour interval is $10^{-4}$ s$^{-1}$.

where $\mathcal{F}$ is an arbitrary function. Two reasons have been proposed why the flow should favor the linear relationship (10). In an inviscid statistical equilibrium model with a finite number of degrees of freedom, (10) is the maximum entropy solution and the most probable one if the flow is ergodic (Salmon et al. 1976). In free-decaying turbulence, Bretherton and Haidvogel (1976) argued that the flow tends toward (10) because it is the solution which has the minimum potential enstrophy for a given energy. This theory relies on the fact that potential entrophy is dissipated much more quickly than energy. Although neight of the two arguments remain valid in strongly forced and dissipative flows, solutions have been found to resemble (10) to a certain extent in barotropic models (Herring 1977; Holloway 1978; Treguier 1989).

In the present case, the mean flow is strongly forced and stratified. However, correlations of nonzonal mean flow and the topography in the bottom layer still agree qualitatively with the steady inviscid solution. Equation (10) implies a correlation of streamfunction and topography at large scales (wavenumbers $K \ll \mu$), and an anticorrelation of relative vorticity $\bar{\zeta}$ and topography at small scales. Those two features appear clearly in the maps of Fig. 4 for case 4L9 (the correlation coefficient with the topography is 0.65 for both $\overline{\psi}_*$ and $-\bar{\zeta}$). Of course, there is a departure from (10) that causes scatter in a plot of $\overline{\psi}_*$ versus $\nabla^2\overline{\psi}_* + \tilde{h}$ (Fig. 5a). The scatter is dependent on the topography. The cases with lower and smaller scale topographies are farther from a linear relationship (Fig. 5b is an example). Generally, (10) is less well satisfied by the large scales of motion, which means that the streamfunction–topography correlation is smaller than the vorticity–topography anticorrelation. For example, the two correlation coefficients are 0.4 and 0.84 for 4L4, and 0.25 and 0.56 for 3L4. It is only with the highest and largest scale topography (cases 4L8 and 4L9) that the two correlation coefficients are approximately equal.

Note that in the present model only the *nonzonal* component $\overline{\psi}_*$ of the mean flow bears some resemblance with the inviscid solution. The steady zonal flow $\langle\bar{\psi}\rangle$ cannot satisfy (10) because of the strong forcing and downward momentum flux, which tends to drive the flow to the east (instead of the west) and gives the zonal flow a sinusoidal structure like that of the wind stress (instead of a uniform one).

To evaluate more quantitatively which part of the flow follows relationship (10), we have tried to separate $\overline{\psi}_*$ in two components. The "correlated" component $\overline{\psi}_c$ similar to (10) is defined by its Fourier transform

$$\overline{\psi}_c(k, l) = \lambda \frac{\tilde{h}(k, l)}{(K^2 + \mu^2)}, \qquad (12)$$

as a function of the wavenumber $(k, l)$ with $K^2 = k^2 + l^2$. The characteristic wavenumber $\mu$ is determined by the condition that the kinetic energy of the residual $\overline{\psi}_r = \overline{\psi}_* - \overline{\psi}_c$ be minimal. An extra constant $\lambda$ is allowed in the definition to make $\overline{\psi}_c$ and $\overline{\psi}_r$ orthogonal in a kinetic energy norm. The percentage of energy accounted for by the "correlated" component $\psi_c$ is given in Table 4. It is non-negligible in all the random

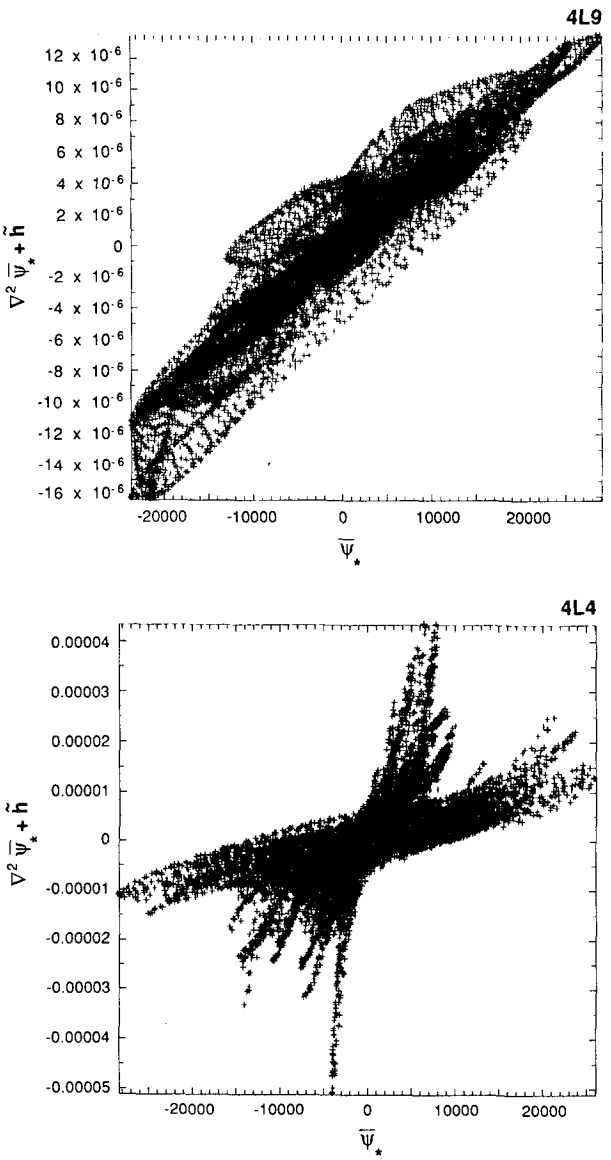


FIG. 5. Scatter plots of $\nabla^2\overline{\psi_*} + \tilde{h}$ vs the nonzonal streamfunction $\psi_*$ at all points of the domain for a case with large scale topography (4L9) and a case with mesoscale topography (4L4).

topography solutions and in some it has quite high values (more than 90%). This separation of streamfunction between $\overline{\psi_c}$ and $\overline{\psi_r}$ is less meaningful for isolated topographies. Considering for example the case of a seamount, $\overline{\psi_r}$ can account for motions trapped around the seamount but not necessarily for standing eddies generated in the lee of the seamount. Despite that fact, for high enough topographies $\overline{\psi_c}$ can account for half the total kinetic energy of $\overline{\psi_*}$ and about a third for the case of a meridional ridge.

This decomposition of the streamfunction shows quantitatively that an important part of the flow adjusts so that the streamfunction is proportional to $(\nabla^2\overline{\psi} + \tilde{h})$. This has two important implications, which will be developed in the following sections. First, the large part of the flow which satisfies (10) has a zero contribution to the domain-averaged topographic form stress. Second, the topographic form stress, Reynolds stress and interfacial form stress are related, as will be shown below in a detailed discussion of the momentum balance.

## 5. Topographic influences on the momentum and energy balances

### a. Momentum balance

Figure 6 shows the momentum balance in layer 1 for the flat-bottom case 4L0 and a case with mesoscale random topography (4L4). The momentum input by the wind is balanced by the interfacial form stress $D_{1+1/2}$, which can be decomposed in two terms:

$$\overline{D_{k+1/2}} = \frac{f_0^2}{g'_{k+1/2}} \left\langle \overline{\psi_k} \frac{\partial}{\partial x} \overline{\psi_{k+1}} \right\rangle$$

$$D'_{k+1/2} = \frac{f_0^2}{g'_{k+1/2}} \left\langle \overline{\psi'_k \frac{\partial}{\partial x} \psi'_{k+1}} \right\rangle . \qquad (13)$$

In the absence of topography, $\overline{D_{k+1/2}}$ is zero because there are no standing eddies, and the downward transfer of momentum is entirely performed by the transient eddies (Fig. 6a). It is no longer true when topography is present. In case 4L4 the standing eddies perform

TABLE 4. Two decompositions of $\overline{\psi_*}$. $\overline{\psi_c}$ is the part of the solution similar to the statistical equilibrium solution, calculated by (12). $\overline{\psi_s}$ is the minimum stress-generating component part of the flow, calculated by (19). The nonzonal kinetic energy integrated over the bottom layer is given in $m^3 s^{-2}$, as well as the percentage accounted for by the two components. $\overline{\psi_c}$ and $\overline{\psi_s}$ are calculated using two different decompositions. Associated with each component is a residual which contains the rest of the kinetic energy.

| Case | Bottom $\overline{K_*}$ | Energy of $\psi_c$ $K_c$ | Energy of $\psi_s$ $K_s$ |
|---|---|---|---|
| 4L1 | 3.3 | 97% | 1.7% |
| 4L2 | 36.7 | 82% | 8.6% |
| 4L3 | 6.1 | 91% | 4.9% |
| 4L4 | 35.6 | 75% | 13.4% |
| 4L5 | 45.6 | 72% | 17.2% |
| 4L6 | 33.5 | 76% | 10% |
| 4L7 | 15.2 | 94% | 3.3% |
| 4L8 | 17.3 | 87% | 7.0% |
| 4L9 | 12.4 | 92% | 4.4% |
| 3L1 | 17.8 | 10% | 8.2% |
| 3L2 | 16.3 | 2% | 4.9% |
| 3L3 | 6.4 | 34% | 35.6% |
| 3L4 | 5.7 | 44% | 30% |
| 3L5 | 8.7 | 45% | 27% |
| 3L6 | 8.6 | 48% | 23.5% |
| 3L7 | 19.7 | 1% | 1% |
| 3L8 | 16.4 | 1% | 2.6% |
| 3L9 | 5.7 | 36% | 3.9% |

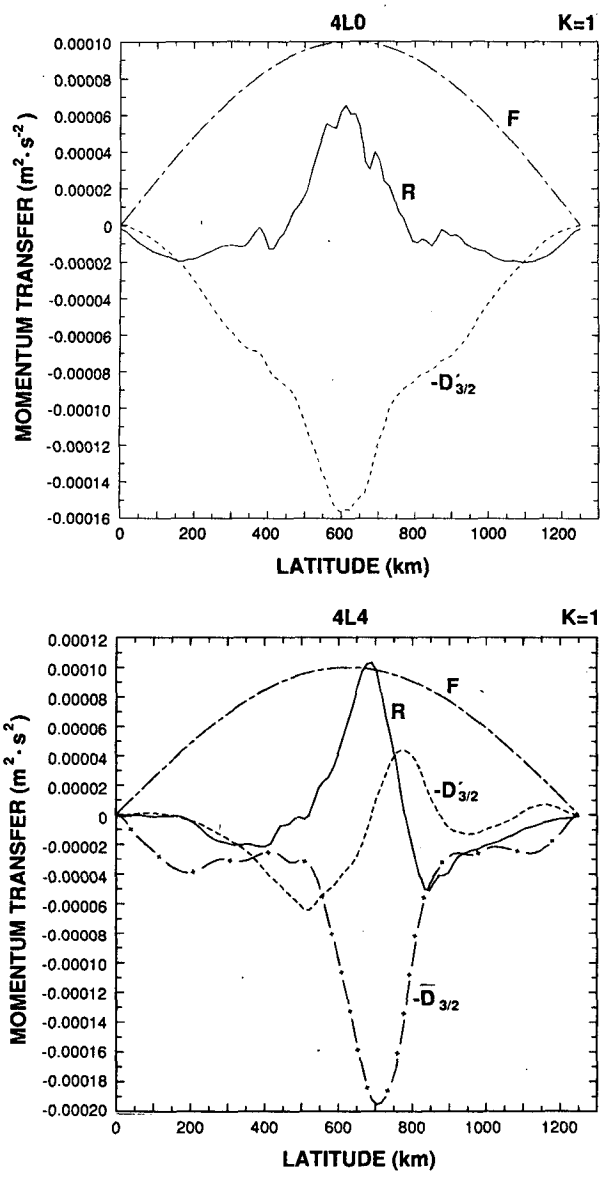


FIG. 6. Momentum balance as a function of latitude in the upper layer for the flat-bottom case 4L0 and case 4L4 with mesoscale topography. The definition of the transfer terms is given in the text. The contribution from the transient eddies $D'$ and standing eddies $\bar{D}$ to the interfacial form stress are shown separately. $\bar{D}$ is zero in the flat-bottom case.

82% of the downward momentum transfer even though their kinetic energy is about five times smaller than the kinetic energy of the transient eddies in the upper layers. The role of the standing eddies has been noted by McWilliams et al. (1978) and Wolff and Olbers (1989), and our solutions show that it varies with the topographic height and shape. With small-scale topography standing eddies are trapped in the bottom layer and have negligible contribution to the downward momentum transport (0% and 3% respectively for cases 4L1 and 4L2). On the other hand, for the large-scale topographies the contribution of the standing eddies is larger than the total downward momentum flux and the transient eddies produce an upward momentum flux. This is true for most 3-layer simulations with isolated topographies.

Lower-layer balances for three cases are shown in Fig. 7 together with the profile of mean zonal velocity. The isolated topography solution (3L6) is particularly simple. The forcing by interfacial form stress is balanced by the topographic form stress near the center of the channel, where the seamount is located. On the sides of the seamount there is only small amplitude random topography and the topographic form stress is negligible, with small-scale variations which reflect the small-scale structure of the topography there. This spatial structure is accentuated in the random topography cases (Figs. 7b and 7c). Instead of being a uniform sink of eastward momentum, the topographic form stress is alternatively a source and a sink, but with eastward forcing the value of the stress integrated in latitude is always negative. The small-scale features are permanent (they do not disappear when diagnostics are calculated over longer time series). In order to obtain a smooth negative curve, one would need to average over many topography realizations or a much longer channel (long compared to the typical topographic scale).

A striking feature of Figs. 7b and 7c is the anticorrelation between the Reynolds stress $\bar{R}$ and the topographic form stress $\bar{T}$ on small meridional scales. A first step in the explanation is to note that zonally averaged Reynolds stresses in the bottom layer are dominated by the contribution from the standing eddies, even in the cases with the lowest topography. It has been shown in the previous section that a large portion of the steady nonzonal streamfunction satisfies

$$\mu^2\overline{\psi_*} = \nabla^2\overline{\psi_*} + \tilde{h}. \tag{14}$$

For that part of the flow, one can write at each latitude line

$$\begin{aligned}\bar{T}(y) = \langle \bar{v}\tilde{h}\rangle &= \left\langle (\mu^2 - \nabla^2)\bar{\psi}\frac{\partial\bar{\psi}}{\partial x}\right\rangle \\ &= \left\langle \mu^2\bar{\psi}\frac{\partial\bar{\psi}}{\partial x}\right\rangle - \left\langle \left(\frac{\partial^2\bar{\psi}}{\partial x^2} + \frac{\partial^2\bar{\psi}}{\partial y^2}\right)\frac{\partial\bar{\psi}}{\partial x}\right\rangle \\ &= -\left\langle \left(\frac{\partial^2\bar{\psi}}{\partial y^2}\right)\frac{\partial\bar{\psi}}{\partial x}\right\rangle = \left\langle \frac{\partial}{\partial y}(\overline{uv})\right\rangle = -\overline{R(y)}. \end{aligned} \tag{15}$$

In the totally inviscid case where (14) is satisfied exactly there is a perfect anticorrelation between the topographic form stress and the Reynolds stress, and both vanish when integrated in latitude:

$$\int \bar{R}(y)dy = \int \bar{T}(y)dy = 0.$$

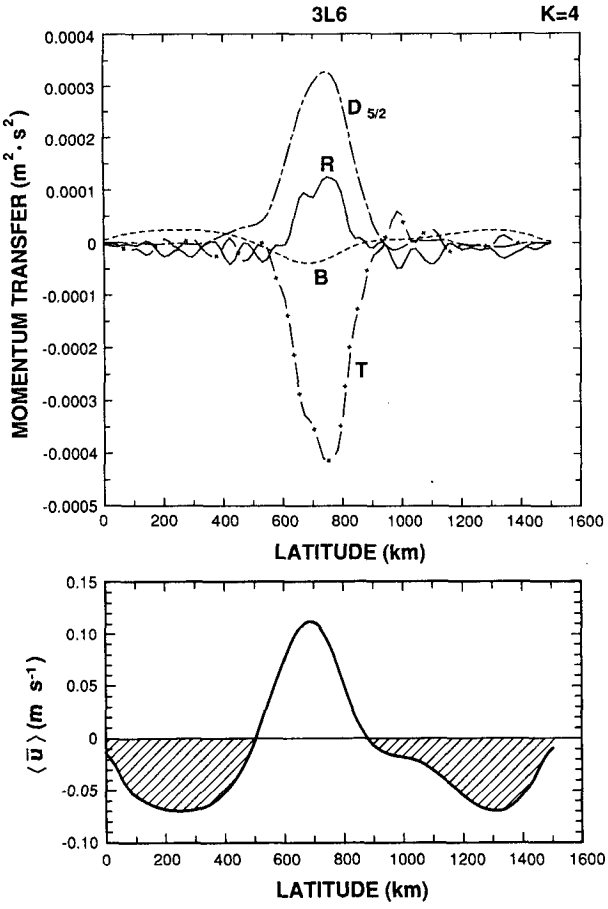


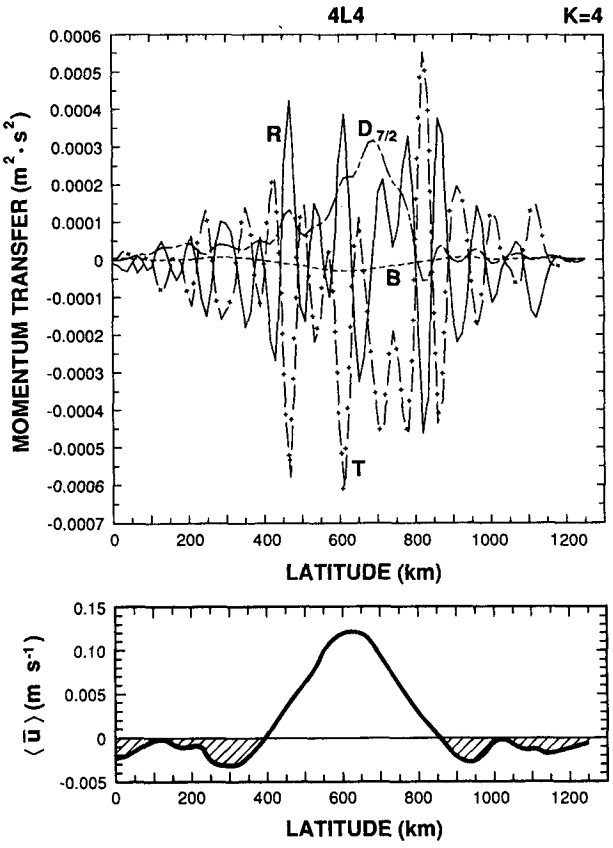


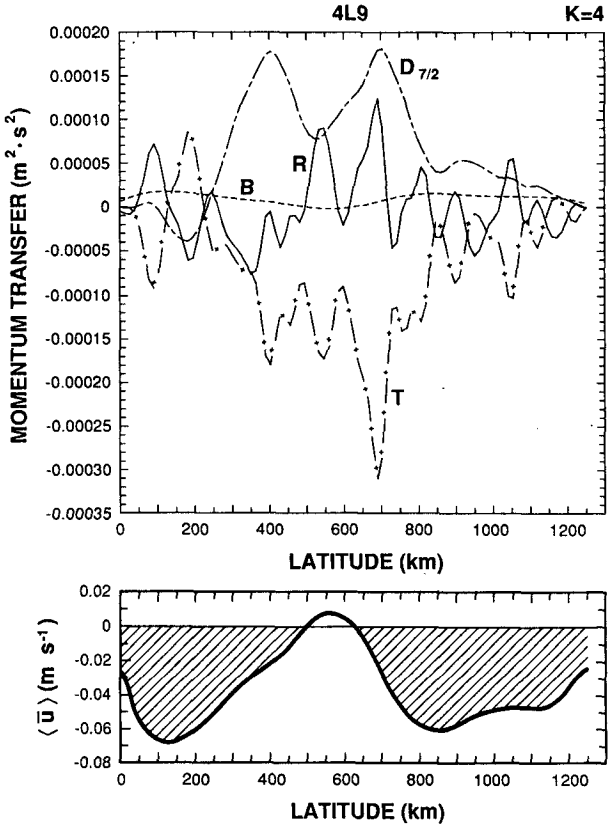


FIG. 7. Momentum balance as a function of latitude in the lower layer for solutions 3L6, 4L4 and 4L9.

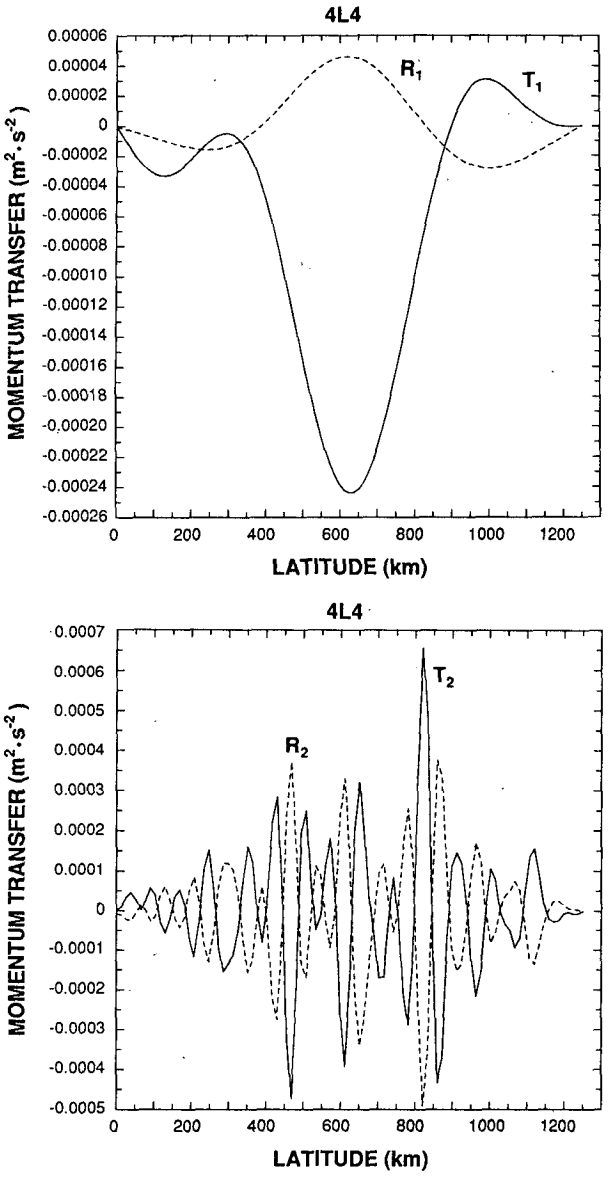


FIG. 8. Low-pass and high-pass filtered topographic form stress and Reynolds stress as a function of latitude for case 4L4.

With forcing and bottom friction, the sum of the Reynolds stresses remains zero whereas the sum of the topographic stress is not. The anticorrelation in (15) is expected mostly at small scales because it arises from the vorticity term in (14). To emphasize that characteristic, $\bar{R}(y)$ and $\bar{T}(y)$ have been decomposed into a large-scale and a small-scale component shown in Fig. 8 for the same case as Fig. 7b. The large-scale component of the topographic form stress can be identified with the low-pass filtered curve $T_1(y)$ of Fig. 8a. It is responsible for the eastward momentum sink: the integrated value of $T_1(y)$ is $-6.24 \times 10^{-5}$ m$^2$ s$^{-2}$, almost balancing the momentum input by the wind ($6.36 \times 10^{-5}$ m$^2$ s$^{-2}$). The small-scale component of the topographic form stress can be identified with the high-pass filtered curve $T_2(y)$ (Fig. 8b). It is anticorrelated with the Reynolds stresses, and tends to redistribute momentum horizontally with a zero net effect. The integrated value of $T_2$ is small (and, in fact, positive): $0.18 \times 10^{-5}$ m$^2$ s$^{-2}$.

A similar anticorrelation exists between the topographic form stress $T$ and the interfacial form stress $D$, but for the large scales. Such a tendency is a consequence of the correlation between the lower interface displacement $\eta_{n-1/2}$ and the topography. Assuming that

$$\overline{\eta_{n-1/2}} = \frac{f_0}{g'_{n-1/2}} (\bar{\psi}_n - \bar{\psi}_{n-1}) \approx \lambda h,$$

$\lambda$ being a positive constant, and assuming that the interfacial form stress in the lower layer is dominated by the standing eddies, one has

$$H_n^{-1} \bar{D}_{n-1/2} = -\frac{f_0^2}{g'_{n-1/2} H_n} \left\langle (\bar{\psi}_n - \bar{\psi}_{n-1}) \frac{\partial \bar{\psi}_n}{\partial x} \right\rangle \approx -\lambda \bar{T}(y). \quad (16)$$

This anticorrelation happens only for topographic scales larger than the Rossby radius.

An interesting feature of the solutions with large-scale topographies is the presence of westward currents in the bottom layer (Figs. 7a and 7c), north and south of the central latitude where the wind stress is maximum. Such currents flowing in the opposite direction of the forcing may happen near the channel walls in flat-bottom solutions. They are usually small (1 cm s$^{-1}$ for 3L0) and they are driven by Reynolds stresses. It is well known that where eddy energy decays *spatially* away from a strongly forced latitude band, Reynolds stresses $R$ tend to generate westward flow on a $\beta$-plane (Rhines 1977). Topography enhances this tendency, and the westward currents on the sides of the seamount in solution 3L6 are larger than in the flat-bottom case (Fig. 7a). Since above the seamount $\bar{T}$ is negative, $R$ is positive because of the anticorrelation discussed above. The integral of $R(y)$ over the channel width must be zero, therefore $R$ must be negative on average on the sides of the seamount and force westward flow there.

In the random, large-scale topography case on the other hand (Fig. 7c), the westward currents flow over large amplitude topography and they are mainly driven by the topographic form stress (although Reynolds stresses locally play a part). Holloway's (1987) barotropic experiments provided the first examples of westward currents driven against an eastward forcing by the topography. The author pointed out that indeed the topographic form stress does not act as a drag (e.g., a force opposite to the direction of the mean flow). Case 4L9 demonstrates that such behavior is also found in stratified flows and that the countercurrents driven by the topography can be strong enough to reverse the

total transport. Such a reversal is possible in the stratified case with a steady eastward forcing because the mean currents can remain eastward in the upper layers. In the barotropic simulations of Holloway (1987), the flow has to reverse at all depths and this is possible only when a random forcing is added, since the mean zonal wind is opposite to the surface flow in that case and can no longer be an energy source.

### b. Energy balance

Important dynamic processes such as instability phenomena are not reflected in the mean momentum balance, and a discussion of energy budgets is necessary to expose them.

The classical energy budgets for quasi-geostrophic models (Holland 1978) show energy exchanges between layers and between the transient and steady flow. There is no topographic transfer term in such a budget, because the topographic effect is confined within the bottom layer, and does not generate a basin-integrated transfer between transient and steady energy:

$$\int\int \overline{J(\psi'_n, h)\psi'_n}\,dxdy = \int\int J(\overline{\psi_n}, h)\overline{\psi_n}\,dxdy = 0.$$

To show the influence of topography, we have calculated energy budgets separating the zonally averaged flow and the standing eddies, as usually done in atmospheric models. The kinetic energy is the decomposed in four terms:

$$K = \langle \bar{K} \rangle + \overline{K_*} + \langle K' \rangle + K'_*,$$

where the time-mean is noted by an overbar, the transients by a prime, the zonal average by brackets and the deviation from the zonal average by an asterisk. The expression of the energy transfer terms is given in the Appendix. In Holland's (1978) energy diagrams, the horizontal dimension is used to separate the transients and time-mean, and the vertical dimension to indicate the layers. Our diagrams (Fig. 9) have a cubic shape, with the third dimension used to separate the zonally averaged from the nonzonal flow. To keep the diagrams readable, only the sum of the three upper layers and the bottom layer are represented in the vertical. Also the potential energy boxes have been suppressed since there is no external source nor sink of potential energy in our model, but the energy transfers involving potential energy conversion are represented as curved arrows to distinguish them from the direct kinetic energy transfers shown as straight arrows.

First we present the energy diagram for a flat-bottom case 4L0 (Fig. 9a) as a reference. It is simple since the time-mean flow is entirely zonal ($\overline{K_*} \approx 0$) and the transients are almost entirely nonzonal ($\langle K' \rangle \approx 0$). The forcing $F$ transfers energy only to the upper layer zonal mean flow. Baroclinic instability tends to generate transients in the upper layer (curved arrow between $\langle \overline{K_s} \rangle$ and $K'_{*s}$) but is partly counteracted by the Reynolds stress intensifying the jet (straight arrow). Transient eddies perform the necessary transfer of energy downward, mainly by their time-mean effect on the zonal mean flow (curved arrow between $\langle \overline{K_s} \rangle$ and $\langle \overline{K_b} \rangle$). The bottom friction $BF$, noted as dashed arrows, is the only significant energy sink. The diagrams are different in the presence of topography mainly because topography transfers energy into the standing eddies ($\overline{TK}$ arrow from $\langle \overline{K_b} \rangle$ to $\overline{K_{*b}}$). For a small-scale topography (Fig. 9b) standing eddies are confined in the bottom layer and only the $\overline{K_{*b}}$ box is involved. With a larger scale topography (Fig. 9c) the interfacial form stress also generates standing eddies in the upper layers (curved arrow between the $\langle \overline{K_s} \rangle$ and $\overline{K_{*s}}$ boxes).

The variability of the zonally averaged flow increases with topography, as shown by the increase of the kinetic energy in the $\langle K' \rangle$ boxes relative to the $\langle \bar{K} \rangle$ boxes in Figs. 9a to 9c. In Fig. 9c, the energy transfers between the transient zonal flow and the others components are not negligible (of order $0.1 \times 10^{-5}$ m$^3$ s$^{-3}$) but have not been represented to improve readability. Those transfers tend to be even larger for larger scale topographies, although the energy content of the $\langle K' \rangle$ boxes remains relatively small (in those cases the transient zonal flow acts like a catalyst for nonlinear interactions). In the bottom layer, transient zonal currents could be generated directly from the transient eddies by a topographic transfer

$$TK' = -\int \overline{\langle u'_b(y) \rangle T'(y)}\,dy,$$

resulting from the correlation of the transient zonal flow $u'_b$ in the bottom layer and the instantaneous value of the topographic form stress $T'$. In contrast with the barotropic model forced by transient winds of Treguier (89), $TK'$ is much smaller than its steady counterpart $\overline{TK}$ in all our solutions even though the fluctuations of the topographic form stress are of the same order as its mean value. In the present stratified model, the transients are generated by baroclinic instability and constrained by the requirement of a downward transfer of energy. This may explain why a correlation between $u'_b$ and $T'$ cannot be maintained at all latitudes and $TK'$ cannot be large. The greater variability of the zonal transport in the presence of topography therefore results from a modification of the instability processes rather than a direct topographic transfer.

The downward transfer of energy is modified in the presence of topography. Since the zonal mean flow decreases, the downward transfer of transient eddy energy becomes larger compared with the downward transfer of mean zonal energy (consider the two vertical curved arrows in Figs. 9a, 9b and 9c). Transients are an essential component of our solutions, which shows their fundamental nonlinear character as opposed to a class

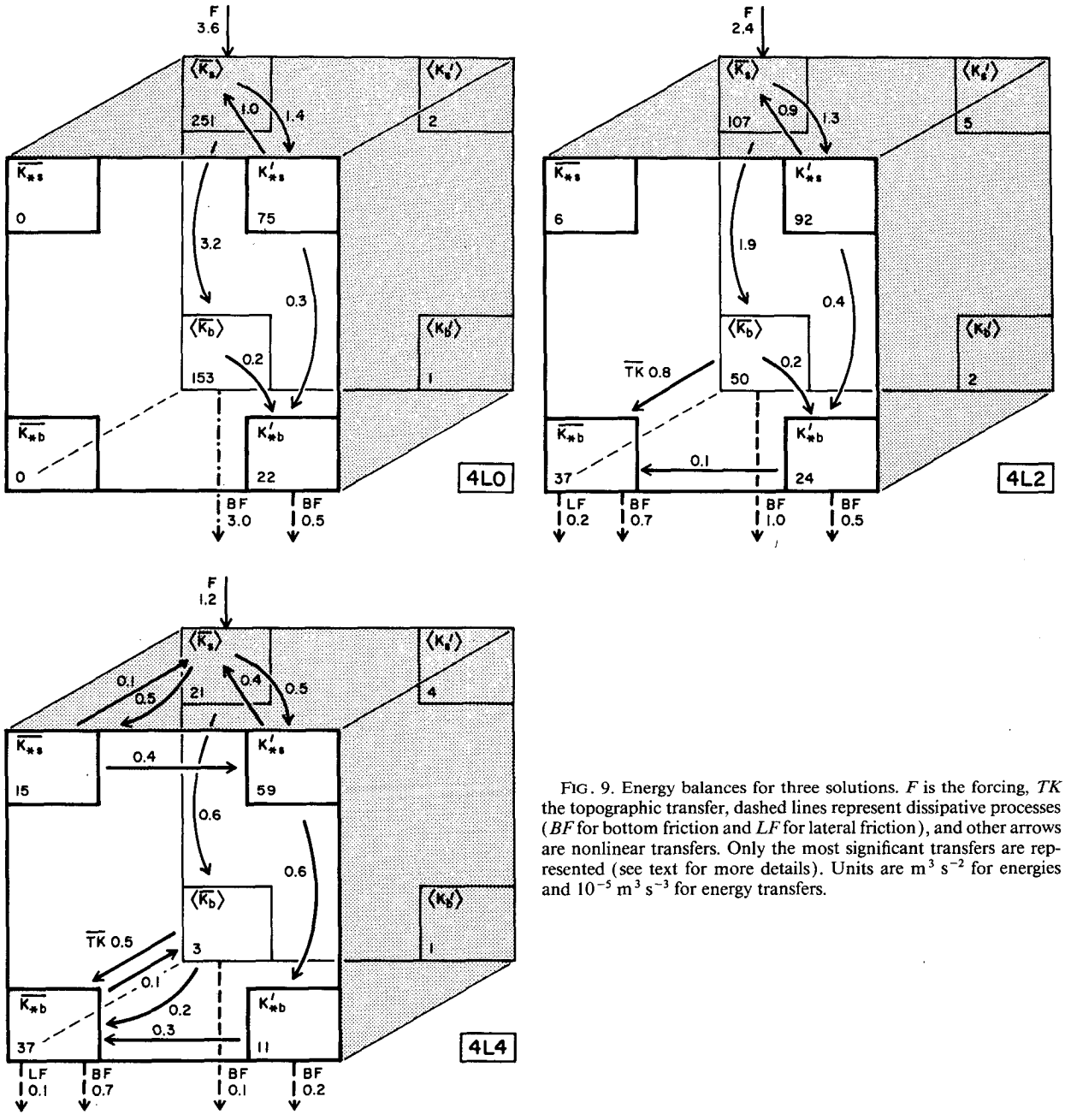


FIG. 9. Energy balances for three solutions. $F$ is the forcing, $TK$ the topographic transfer, dashed lines represent dissipative processes ($BF$ for bottom friction and $LF$ for lateral friction), and other arrows are nonlinear transfers. Only the most significant transfers are represented (see text for more details). Units are $m^3\ s^{-2}$ for energies and $10^{-5}\ m^3\ s^{-3}$ for energy transfers.

of weakly nonlinear models of zonal flow–topography interactions in the atmosphere (e.g., Charney and Strauss 1980). The latter models can achieve a completely steady solution because there is forcing and damping in all the layers. It is not the case in our model, where energy must be transferred downwards. Although there is a downward transfer of *momentum* due to the standing eddies, it is easily demonstrated that standing eddies cannot perform a vertical transfer of *energy* (see the Appendix). In many of our simulations with large-scale topography (3L4, 3L6, 3L9 for example), standing eddies contribute significantly to the downward transfer between $\langle \overline{K_s} \rangle$ and $\langle \overline{K_b} \rangle$. Therefore, in those cases (not shown) there is a compensating upward transfer of energy between $\overline{K_{*b}}$ and $\overline{K_{*s}}$.

Stability properties of the standing eddies can be inferred from the energy transfers between $\overline{K_*}$ and $K'_*$. In the energy balance for case 4L4 (Fig. 9c), the energy transfer in the upper layers is from the standing eddies to the transients whereas it is opposite in the lower layer. This happens in most of our solutions. Energy transfers in the upper layers reveal a barotropic instability of the standing eddies. This is not surprising, since topographically generated stationary waves in barotro-

pic models have been shown to be linearly unstable in a wide range of circumstances (e.g., Charney and de Vore 1979). In case 4L4 (Fig. 9c), this barotropic instability is a mechanism as important as the baroclinic instability of the mean zonal flow in forcing the transients. This explains why the spatial structure and time scale of the transients are modified in the presence of topography. The reverse direction of the energy transfer between $\overline{K_{*b}}$ and $K'_{*b}$ on Figs. 9b and 9c shows that although barotropic instability may still be present, it is not the dominant mechanism in the bottom layer. The main energy transfer is a rectification mechanism, similar to the one pointed out in free decaying turbulence by Bretherton and Haidvogel (1976). The efficiency of the rectification process has been demonstrated in the case of barotropic turbulence forced by transient winds by Herring (1977), Haidvogel and Brink (1986), and Treguier (1989). The present solutions extend those results to the lower layer of a steadily forced baroclinic model. Rectification is an important forcing mechanism for $\overline{K_{*b}}$, and sometimes the most important one, for the solutions with random topography filling the domain. It is generally smaller in the cases with isolated topography. This suggests that the rectification mechanism operates locally above topographic features.

Finally, the energy balances for the highest and largest scale topographies (4L9 for example) show a reversal of the topographic form stress energy transfer $\overline{TK}$, from the standing eddies to the zonal mean:

$$\overline{TK} = -\int \langle \overline{u_b(y)} \rangle \bar{T}(y) dy < 0.$$

The sign of the transfer $\overline{TK}$ depends on the correlation between the steady zonal flow $\langle \overline{u_b(y)} \rangle$ and the topographic momentum stress $\bar{T}(y)$. Usually, $\langle \overline{u_b(y)} \rangle$ is positive (eastward flow), $\bar{T}$ is negative, and $\overline{TK}$ transfers energy from the zonal averaged flow to the standing eddies. For case 4L9, $\langle \overline{u_b(y)} \rangle$ is westward and $\bar{T}$ is negative in the most part of the channel (Fig. 7c). Here $\overline{TK}$ is reversed, expressing the fact that the topographic stress is accelerating the zonal westward flow as discussed in the preceding section.

## 6. Mass transport and volume-integrated momentum balance

### a. *Mass transport variability*

Energy balances show that the time variability of the transport is negligible in the flat-bottom case ($\langle K' \rangle \approx 0$) but is enhanced in the presence of topography. The fluctuations have long time scales, as shown in Fig. 10 for the case of a seamount with maximum height 1000 m (3L4). This case presents especially large variations but it is nonetheless representative of the other 3-layer cases. The amplitude of the fluctuations and their time scale are generally smaller for the random topographies.

The sequence of transport variations near the end of the time series displayed in Fig. 10 is especially striking. The transport remains close to 300 Sv during about 500 days, changes abruptly to a value close to −200 Sv, and oscillates about this value for about 500 days again. By analogy with atmospheric models, one could say that the flow is in an "unblocked" state during the first period, with zonally oriented streamlines and a low topographic form stress, and in a "blocked" state during the second period, since a reversal of the transport requires a large amplitude of the standing eddies and a large topographic form stress. Indeed, the flow patterns agree with that terminology.

In the present model, the large variations of the transport are probably dependent on the channel length compared to the maximum topographic wavelength. Averaging over more topographic length scales would reduce the amplitude of the oscillations. The relatively small time variability of the transport in Drake Passage (Nowlin and Klinck 1986) may reflect the fact that the Antarctic Circumpolar current flows over many large-scale topographic features. This contrasts with atmospheric models, where the topographic influences are dominated by low wavenumbers (contrast between oceans and continents). Zonal winds vary considerably in relation with blocking events, and topography has been suggested as a possible cause of that variability (Charney and De Vore 1979).

Because of the long time scale of the fluctuations, it is necessary to obtain very long series in order to get a reliable estimate of the time-mean transport. Table 5 gives the time-mean transport for all our cases with an estimate of its uncertainty. The latter is based on

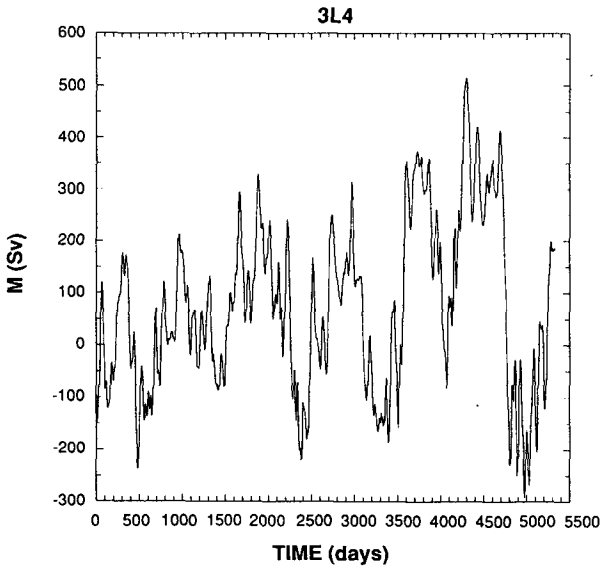


FIG. 10. Time series of the total transport for case 3L4 with an isolated seamount of maximum height 1000 m.

TABLE 5. Transport and momentum balance. $\epsilon$ is the uncertainty associated with the mean total transport (see text). The momentum balance in the lower layer involves the downward transfer of energy (equal to the surface wind stress provided biharmonic friction is negligible), the bottom friction and the topographic stress. The last two terms are given as percentages of the wind stress momentum forcing, which is $6.37 \times 10^{-5}$ m$^2$ s$^{-2}$ for 4-layers solutions and $5 \times 10^{-5}$ m$^2$ s$^{-2}$ for 3-layers solutions.

| | Transport (Sv) | | | Momentum balance | |
|---|---|---|---|---|---|
| Case | Total | $\epsilon$ | Lower layer | Topography | Bottom friction |
| 4L0 | 1859 | ±3 | 796 | 0 | −100 |
| 4L1 | 1756 | ±4 | 761 | −5 | −95 |
| 4L2 | 1060 | ±21 | 396 | −50 | −50 |
| 4L3 | 1460 | ±11 | 614 | −22 | −77 |
| 4L4 | 275 | ±12 | 47 | −95 | −5 |
| 4L5 | 650 | ±13 | 231 | −71 | −29 |
| 4L6 | 739 | ±14 | 266 | −66 | −34 |
| 4L7 | −47 | ±14 | −98 | −113 | +12 |
| 4L8 | 52 | ±21 | −32 | −104 | +4 |
| 4L9 | −91 | ±13 | −119 | −114 | +15 |
| 3L0 | 1246 | ±1 | 750 | 0 | −100 |
| 3L1 | 830 | ±18 | 466 | −37 | −62 |
| 3L2 | 698 | ±23 | 373 | −51 | −49 |
| 3L3 | 60 | ±25 | −64 | −108 | +8 |
| 3L4 | 73 | ±44 | −54 | −106 | +7 |
| 3L5 | 38 | ±24 | −78 | −110 | +10 |
| 3L6 | 1 | ±22 | −93 | −113 | +12 |
| 3L7 | 813 | ±14 | 455 | −40 | −60 |
| 3L8 | 246 | ±28 | 69 | −91 | −9 |
| 3L9 | −11 | ±7 | −73 | −110 | +10 |

the standard deviation, divided by the square root of the number of degrees of freedom computed using the average time scale (inverse of the center of gravity of the frequency spectrum). The typical time scale for the transport variations is always greater than 100 days and reaches 400 days in solution 3L4. Although the time-mean has been computed on time series of 2000 days or longer, the uncertainty remains large, or order ±30 Sv for the isolated topographies and ±15 Sv for the random topographies.

### b. *Transport as a function of topography*

The values in Table 5, plotted in Fig. 11 for the 3-layer cases, show the great sensitivity of the transport to the topographic height and shape. The transport is also dependent of other parameters, which are not studied in detail here (forcing, bottom friction, stratification and $\beta$-effect). For all the different kinds of topography the behavior of the transport is similar when the topographic height increases from zero. There is a rapid decrease of the transport, until the topographic form stress has almost completely replaced bottom friction in the momentum budget and the transport has become close to zero. Then, any further increase of the topographic height has smaller effects. The transport may decrease to become negative, but does not seem to be able to reach very large negative values. Between cases 4L7 and 4L8 and 3L3 and 3L4, respectively, the rms topographic height is doubled but the transport does not vary significantly. The "critical" topographic height at which the topographic form stress is almost equal to the wind stress forcing varies according to the shape and horizontal scale of the topography. For the random topographies, the largest scale topographies are the most efficient in generating a large topographic form stress, and do not need a large rms height to reduce the transport. For the isolated topographies, the meridional ridges are more efficient than the seamounts, which matches our intuition that flow will easily go around seamounts but be blocked by a ridge. Generally, for the same rms height, an isolated seamount or ridge situated in the middle of the channel provides a larger form stress than a random topography.

Our solutions, where the form stress is largest for the largest scale topographies, are different from the barotropic solutions forced by transient winds of Treguier (1989). In the latter case the largest topographic form stress $\bar{T}$ occurs for intermediate topographic scales (topographies with an rms slope $\alpha$ comparable with $\beta H/f_0$). The decrease of $\langle \bar{v}\tilde{h} \rangle$ for large-scale topographies is a secondary effect due to a decrease of $\bar{v}$ (e.g., a decrease of the energy of the standing eddies), itself due to a smaller rectification process. In Treguier (1989), the nonlinear energy transfer between $K'_*$ and $\overline{K_*}$ is the only energy source for the standing eddies and it is smaller for large-scale flows. In the present solutions on the other hand, the standing eddies draw energy from the steadily forced zonal flow and $\overline{K_*}$ grows when the topographic spatial scale increases. Therefore,

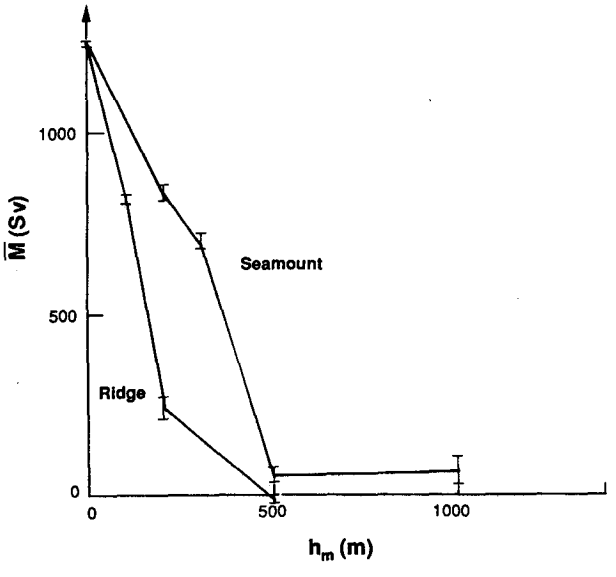


FIG. 11. Total transport as a function of the topographic maximum height $h_m$ for the isolated seamounts and ridges cases. The bars represent the uncertainty (see Table 5).

no decrease of the topographic form stress for large-scale topographies is observed.

### c. *Spectral decomposition of the domain-averaged topographic form stress*

To understand why larger scale topographies generate a larger topographic form stress, it is useful to examine the contribution from various spatial scales to the domain-averaged topographic form stress $\bar{T}$ by looking at its expression in wavenumber space

$$\bar{T} = -\int\int \bar{\psi}(x, y)\frac{\partial \tilde{h}}{\partial x}(x, y)dxdy$$

$$= \mathrm{Re}\int\int \bar{\psi}(k, l)ik\tilde{h}^c(k, l)dkdl$$

$$= \int A_K(K)C_K(K)dK. \qquad (17)$$

The same notation is used for a function and its Fourier transform for simplicity, $i = \sqrt{-1}$, $c$ denotes a complex conjugate and $\|$ the norm of complex number; $A_K$ and $C_K$ are defined by

$$A_K = \sum_{\sqrt{k^2+l^2}=K} |k\bar{\psi}\tilde{h}|$$

$$C_K = A_K^{-1}\,\mathrm{Re}\Big(\sum_{\sqrt{k^2+l^2}=K} ik\bar{\psi}\tilde{h}^c\Big) \qquad (18)$$

where $A_K$ represents the "amplitude" contribution to the topographic form stress, e.g., the product of the amplitudes of $\bar{\psi}$ and $\partial\tilde{h}/\partial x$ in the wavenumber band $K$ and $C_K$ is a "phase" contribution to the topographic form stress (the correlation coefficient of $\psi$ and $\partial\tilde{h}/\partial x$ averaged over wavenumber band $K$).

In all our cases, the total integrand $A_KC_K$ is larger for large scales. In the example of Fig. 12a, the integral in (17) converges to the total value of $\bar{T}$ when wavelengths greater than 400 km are included. In fact, in all our solutions we find that the components $A_KC_K$ associated with wavelengths larger than 417 km (or 500 km in the 3-layer cases with a wider channel) account for at least 90% of the total topographic form stress, excepted of course for the cases where there is no topography with wavelengths larger than 417 km.

The importance of the large scales can be understood by considering separately $A_K$ and $C_K$. The amplitude contribution depends on the shape of the streamfunction spectrum and the topographic slope spectrum. With a $K^{-2}$ topography, the slope spectrum is white, but the streamfunction spectrum is always red mainly because of the large scale forcing, making $A_K$ a decreasing function $K$. The topographic spectrum flattens out at large scales for our cases 4L7 and 4L8 as well as with isolated topographies, but the redness of the $\bar{\psi}$ spectrum is sufficient to ensure that $A_K$ is weighted towards large scales, even if it is no longer monotonically decreasing.

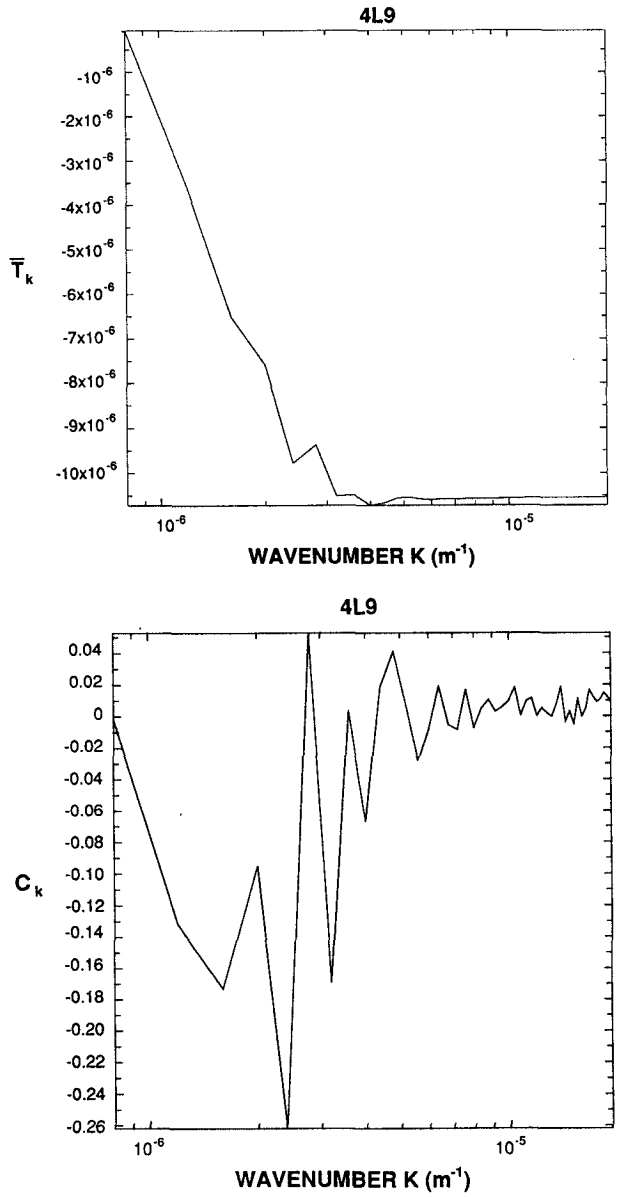


FIG. 12. Wavenumber decomposition of the domain-averaged topographic form stress $\bar{T}$ for solution 4L9 with large scale topography. (a) Sum $T_K$ of the contributions to $\bar{T}$ between wavenumbers $\kappa = 0$ and $\kappa = K$ (see text) as a function of the wavenumber $K$ (expressed as an inverse wavelength in $m^{-1}$). Units for $T_K$ are nondimensional. (b) Phase contribution $C_K$ to the domain-averaged topographic form stress (defined in the text) as a function of wavenumber $K$.

The phase contribution $C_K$ reinforces that tendency. For all $K$, $C_K$ is very small. The sum of the amplitudes $A_K$ alone is at least one order of magnitude larger than the actual topographic form stress (sum of the products $A_KC_K$). This is not surprising since we have demonstrated in section 4 that a large part of the flow resembles the inviscid steady solution (10), for which $C_K$ is exactly zero. Furthermore, the amplitude of $C_K$ tends to decrease with $K$. This merely reflects the fact that

the correlation of the streamfunction with the topography at large scales is smaller than the anticorrelation of vorticity with topography at small scales, a feature which has been discussed in section 4. An example of $C_K$ for case 4L9 is shown in Fig. 12b. Notice that $C_K$ is not necessarily negative for all wavenumbers (a negative value of $C_K$ corresponds to a westward phase shift of the streamfunction relative to the topography, hence a westward stress). However, $C_K$ is negative on average, ensuring that the domain-integrated topographic form stress is negative. Although the curve in Fig. 12b is noisy, it clearly shows that $C_K$ is small for the high wavenumbers.

The predominance of the large scales (of the order of the forcing scale) in the domain-averaged topographic form stress is a robust feature of all our solutions. The main reason is that with large-scale forcing the spectrum of the mean streamfunction is red (dominated by large scales), and a secondary reason is that small scales adjust to a quasi perfect vorticity–topography anticorrelation which prevents any contribution to the form stress. However, this predominance may not persist in different parameter regimes. For example, we have not explored quasi-linear regimes in which $\beta L^2/u \geqslant 1$. Also, if the forcing had a smaller spatial scale, the contribution of the large scales could be diminished because then the spectrum of $\bar{\psi}$ would have a peak at intermediate scales. A solution has been calculated similar to 3L1 but with the width of the forcing function reduced to one third of the channel width. The mean streamfunction spectrum has a peak at wavelength 750 km, but it is not enough to break the above "rule" that wavelengths larger than 500 km account for 90% of the total form stress.

### *d. Influence of small-scale topography*

From the preceding section one would be tempted to conclude that small-scale topography has a negligible effect on the flow. It is not true, because even though small scales do not contribute to the domain-averaged topographic form stress, they may affect it indirectly by modifying the dynamics of the large scale flow. Such an indirect effect of the small topographic scales is demonstrated by two series of experiments.

In the case of random topography, solution 4L6 has the same parameters as 4L4 but topographic wavelengths smaller than 208 km have been filtered out. The small scales contribute significantly to the rms height in a $K^{-2}$ spectrum, since the value of $h$ rms is decreased from 400 to 297 m when the spectrum is truncated. From that consideration alone one might expect the two cases to be different. Indeed, the transport is twice as large for 4L6 as for 4L4, and the topographic form stress is reduced to 71% of the wind stress instead of 95% (Table 5). In both solutions the domain-integrated form stress is entirely due to wavelengths between 208 and 417 km. However, in 4L4 the presence of smaller wavelengths affects the larger scales so that the value of the form stress is increased. The two cases are qualitatively different, and it is difficult to infer from the energy or momentum balances how the small-scale topography influences the flow. The zonal mean flow has four times less kinetic energy in 4L4 compared with 4L6, so one may assume that the presence of small-scale topography favors the instability mechanisms. In some respects case 4L6 with truncated topography is closer to another solution in which small-scale topography is retained (same spectrum as 4L4) but the rms height is only 297 m (case 4L5). The total transports are similar: 650 Sv for 4L5 and 739 for 4L6 (Table 5). This would suggest that one could increase the height of the retained topographic scales in order to account for the unresolved variability in the topographic field, as sometimes done in atmospheric models by the use of the so-called "enveloppe" orography. However, this has not been systematically investigated, since trying to parameterize nonresolved topographic effects is certainly premature in the present state of oceanic models.

The comparison of case 3L3, with an isolated seamount, and cases 3L5 and 3L6, in which small-scale random topography has also been added, gives similar results. In 3L5 the random topography has a maximum wavelength of 250 km, and there is a spectral gap between the isolated seamount and the random noise. This case is not very different from the isolated seamount case 3L3, excepted for the increase of relative vorticity in the bottom layer in 3L5 and the larger vorticity–topography correlation coefficient (0.83 instead of 0.54). In case 3L6 there is no spectral gap between the seamount and the random topography, and although the latter has a rms height of only 50 m, it reduces significantly the transport (from 60 Sv in 3L3 to almost zero in 3L6). Note that the topographic form stress increases only by 5% between those two solutions. The large effect on the transport is explained by looking at the simple equation (7), which shows that the bottom layer transport $M_n$ is given by the sum of the integrated forcing $F$ and topographic form stress $T$ divided by the bottom friction coefficient. In the regime where $-T$ almost equals the forcing, a variation of $T$ of a few percent can decrease the transport by a factor of 10 as happens between 3L3 and 3L6.

## 7. Spatial structure of the topographic form stress

### *a. Comparison of $\bar{v}\tilde{h}$ and $\bar{\psi}\partial\tilde{h}/\partial x$*

The momentum balances as a function of latitude show that $\bar{T}(y)$ has a small-scale structure, but only the large scales appear to influence the transport. In the present section, we extend this analysis to two dimensions (zonal and meridional).

The topographic form stress is uniquely defined as a zonal mean, but there is some arbitrariness in defining its pointwise value, e.g. the integrand for the zonal in-

tegral. In a quasi-geostrophic model, the same value of $\bar{T}(y)$ is obtained using either $\overline{T_v}(x, y) = \bar{v}\tilde{h}$ or $\overline{T_p}(x, y) = -\bar{\psi}\partial\tilde{h}/\partial x$ as an integrand. In a more general fluid dynamics model, the most familiar expression for $\bar{T}(y)$ is

$$\bar{T}(y) = -\int \frac{\bar{P}}{\rho H}\frac{\partial h}{\partial x}\,dx$$

where $P$ is the pressure. This form of the integrand is equal to $\overline{T_p}(x, y)$ in the quasi-geostrophic approximation.

We compare plots of $\overline{T_p}(x, y)$ and $\overline{T_v}(x, y)$. First, let us consider the case of an isolated mountain (3L3) in Fig. 13. Here $\overline{T_p}(x, y)$ and $\overline{T_v}(x, y)$ have the same simple structure, with two zones of different sign on each side (east or west) of the topography, corresponding to different signs of either $\partial\tilde{h}/\partial x$ or $v$. The negative part is the largest in both cases, because the high pressure (minimum of $\psi$ since $f$ is negative) lying over the topography is shifted westward of the obstacle due to the eastward mean flow. Adding a small-scale topography completely changes the picture (case 3L6, Fig. 14). The spatial structure of $\overline{T_p}(x, y)$ is very different and small scale, whereas the structure of $\overline{T_v}(x, y)$ is still close to the simple double-lobe shape of case 3L3. Part of the noise in the structure of $\overline{T_p}(x, y)$ is due to the product of the zonal average of $\langle\bar{\psi}\rangle$ with the small scales in $\partial\tilde{h}/\partial x$, as suggested by the bandlike structure of the noise near the channel walls. However, removing the zonal average of $\bar{\psi}$ before calculating $\overline{T_p}(x, y)$ (which does not modify the zonally integrated topographic stress) does not change its typical spatial scale, which remains smaller than for $\overline{T_v}(x, y)$ (Fig. 14c).

The difference between the spatial scales of $\overline{T_v}(x, y)$ and $\overline{T_p}(x, y)$ appears in all our cases where some random topography is present. It is simply due to the fact that the spectrum of $\bar{\psi}$ is steeper than the spectrum of $\tilde{h}$. Products in physical space are convolutions in spectral space. The convolution of $\bar{v}$ and $\tilde{h}$ involves two moderately steep spectra and is also moderately steep, with horizontal scales close to those of both $\bar{v}$ and $\tilde{h}$. On the other hand, the convolution of $\bar{\psi}$ and $\partial\tilde{h}/\partial x$ involves a very red spectrum and a rather flat one. In that case, the spectrum of the convolution has a shape similar to the flat spectrum, and therefore the spatial scales of $\overline{T_p}(x, y)$ are close to the spatial scales of $\partial\tilde{h}/\partial x$.

This contrast between $\overline{T_p}(x, y)$ and $\overline{T_v}(x, y)$ may be expected to hold in many situations, since generally the spectrum of $\bar{\psi}$ tends to be steeper than the spectrum of $\tilde{h}$. Exceptions could be regions of very smooth topography, or western boundary currents where $\bar{\psi}$ has small spatial scales. It suggests that if measurements of the topographic form stress were made, it would be easier to obtain a reasonable average with only a limited number of point measurements by measuring $\bar{v}\tilde{h}$ instead of $-\bar{P}\partial h/\partial x$.

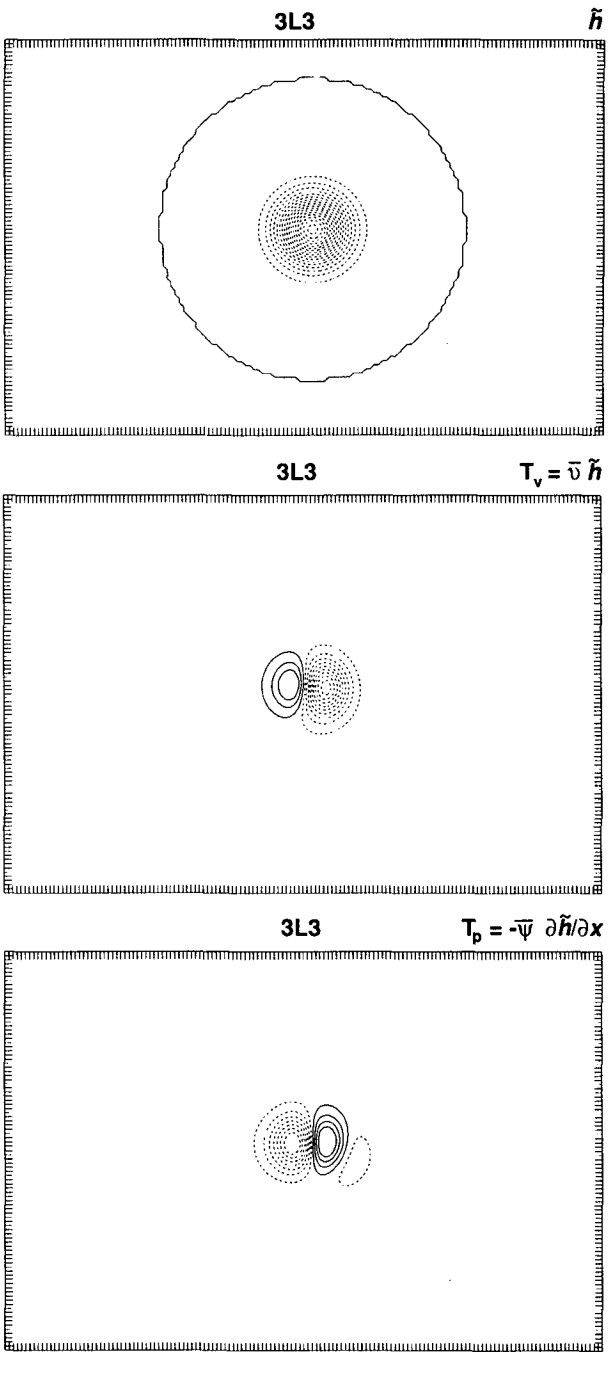


FIG. 13. (a) Topography $\tilde{h}$ for solution 3L3 (contour interval is $0.9\ 10^{-6}\ s^{-1}$). (b) $\bar{v}\tilde{h}$ (c.i. is $0.4 \times 10^{-6}\ m\ s^{-2}$). (c) $-\bar{\psi}\partial\tilde{h}/\partial x$ (c.i. is $0.5 \times 10^{-6}\ m\ s^{-2}$).

### b. *Isolation of the stress-generating component*

The small-scale structure of the topographic form stress is associated with the part of $\bar{\psi}$ which is correlated with the topography (see section 5). An attempt has been made in section 4 to quantify which part of the flow is close to a statistical equilibrium solution. The

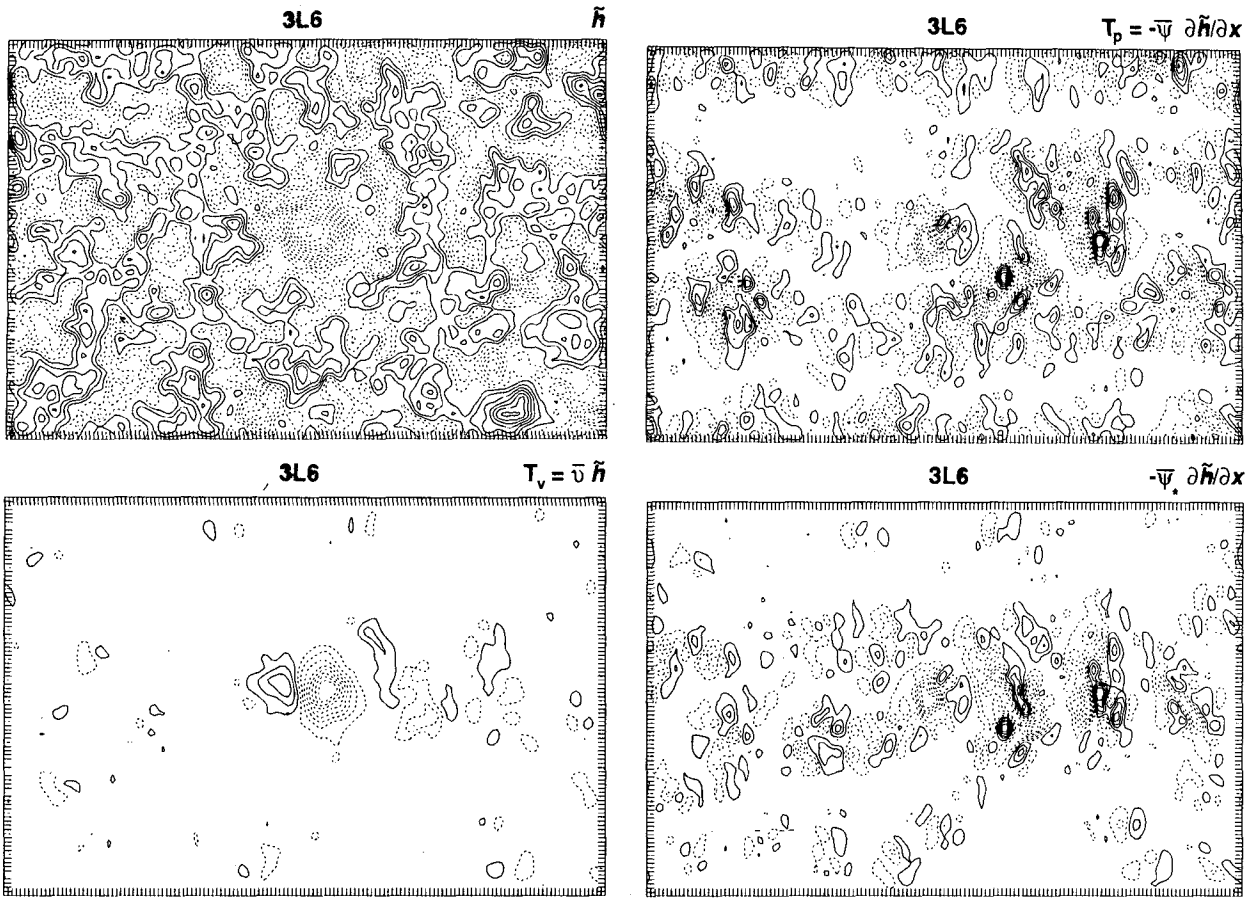


FIG. 14. (a) Topography $\tilde{h}$ for solution 3L6 (contour interval is $1 \times 10^{-6}$ s$^{-1}$). (b) $\overline{v}\tilde{h}$ (c.i. is $0.3 \times 10^{-6}$ m s$^{-2}$). (c) $-\overline{\psi}\partial\tilde{h}/\partial x$ (c.i. is $0.4 \times 10^{-6}$ m s$^{-2}$). (d) $-\overline{\psi_*}\partial\tilde{h}/\partial x$ (c.i. is $0.3 \times 10^{-6}$ m s$^{-2}$).

residual $\overline{\psi_r}$ in that decomposition is an estimate of the part of the flow which contributes to the domain-integrated topographic form stress. However, it is not the best possible estimate. The stress-generating component of $\overline{\psi_s}$ can be evaluated directly in wavenumber space. For each wavenumber $(k, l)$ it satisfies

$$\overline{\psi_s}(k, l) = iC(k, l)\tilde{h}(k, l). \qquad (19)$$

$C(k, l)$ is defined as

$$C(k, l) = \mathbf{R}\mathrm{e}(ik\overline{\psi_*}\tilde{h}^c)/k|\tilde{h}^2|,$$

where Re is the real part, $c$ is the complex conjugate and $|\ \ |$ is the norm of a complex number. The percentage of the total bottom layer kinetic energy $\overline{K_{*b}}$ accounted for by the $\overline{\psi_s}$ component is indicated in Table 4 to allow a comparison with the fitting to the steady inviscid solution (10). This alternative decomposition confirms that a *very* small part of the flow contributes to the domain averaged topographic form stress. It can be as small as 5 or 10% for the random topography cases, and is typically about 30% for the isolated topography cases. An example of the decomposition for 4L9 is given in Fig. 15. $(\overline{\psi_*} - \overline{\psi_s})$ is in phase with the topography (which is plotted in Fig. 4a) and contain most of the kinetic energy. $\overline{\psi_s}$ is out of phase with the topography, has larger spatial scales and contains only 4.4% of the kinetic energy. In fact, the components $\overline{\psi_c}$ and $\overline{\psi_r}$ resulting from the other decomposition (12) introduced in section 4 have very similar spatial structures.

This result implies that measurements of the topographic form stress have the further complication of a small signal/noise ratio ($\overline{\psi_s}$ being the signal). In the near future, $\bar{T}$ will probably have to be evaluated by indirect techniques (as a residual in the momentum balance) rather than measured directly.

## 8. Conclusion

In the present paper, topographic influences on a channel flow have been studied from a statistical point of view. We have not tried to imitate the real geometry of the Antarctic Circumpolar Current. Instead, we have used a small rectangular domain allowing us to perform

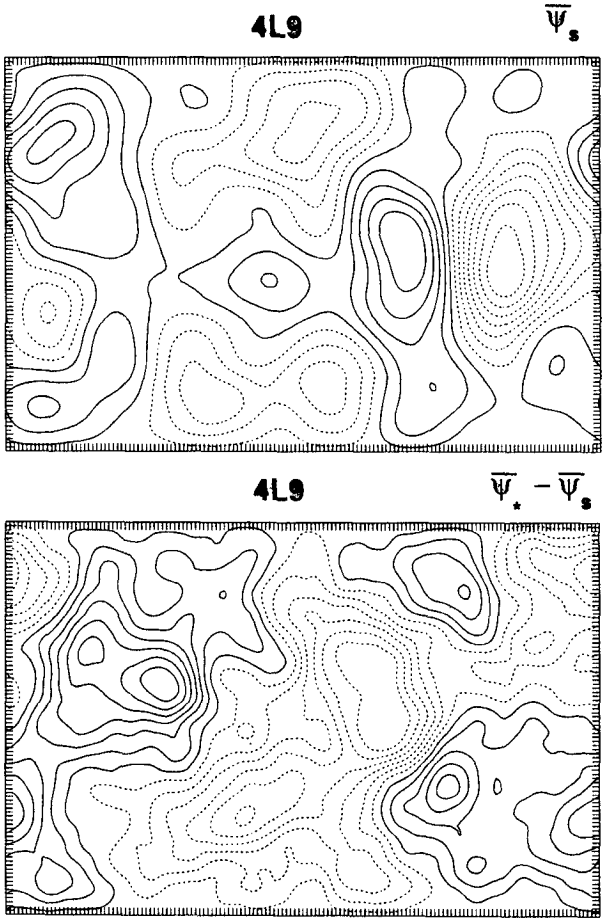


FIG. 15. Decomposition of $\overline{\psi_*}$ according to (19) for solution 4L9. (a) Stress-generating component $\overline{\psi}_s$, (b) Residual $\overline{\psi_*} - \overline{\psi}_s$. Contours intervals are 1000 and 4000 $m^2 s^{-1}$, respectively.

a large number of simulations with good horizontal and vertical resolution.

The effect of topography on a steady-forced channel flow has traditionally been described in terms of the momentum balance. Our results confirm that even low topographies (rms heights of about 200 m) can generate a large form stress and replace bottom friction in the momentum budget. For the same rms height, an isolated feature in the path of the jet is more efficient than a randomly distributed topography, and a meridional ridge affects more the transport than a seamount of limited latitudinal extent. Once the transport has been reduced so that bottom friction is small compared to the forcing, further increase of the topographic height has little effect on the transport. In the present case of forcing by eastward winds, the topographic form stress can not only remove eastward momentum but even force a westward flow, and we show examples of westward countercurrents driven by the topographic form stress below a surface wind-forced eastward flow. Holloway (1987) has suggested that coastal countercurrents like the California undercurrent may be driven by a similar mechanism.

Analysis of space, time scales, and correlations of the flow with the topography provide a new picture of the topographic influence. The standing eddies correlated with the topography are either trapped in the bottom layer for small-scale topography, or penetrate higher in the water column according to the ratio of the topography length scale to the Rossby radius of deformation. A large part of the bottom layer steady flow adjusts so that relative vorticity and topography are anticorrelated at small scales, and the streamfunction and topogrpahy are correlated at large scales although to a smaller extent. This behavior is similar to the statistical equilibrium solution valid for inviscid flows with a finite number of degrees of freedom. An important consequence is that the flow correlated with the topography does not generate any topographic form stress in the bottom layer. A minimum stress-generating component is calculated, and is found to contain only 5% to 10% of the kinetic energy in the random topography cases, and about 30% in the isolated topography cases. Also, the topographic form stress $\bar{T}$ is anticorrelated with the Reynolds stress at small scales because of the vorticity–topography anticorrelation.

When the topographic horizontal scale is large and produces a permanent deformation of the upper layer interfaces, the interfacial form stress is correlated with the topographic form stress. In that case the standing eddies rather than the transients transfer momentum downward. In a recent paper Johnson and Bryden (1989) suggest a simple momentum balance for the ACC, assuming that all the momentum input by the wind stress is transferred downwards by the transients and removed by the topographic form stress. This is probably an incomplete picture. Standing eddies cannot be neglected in the momentum balance of the ACC, because it flows over large-scale topography.

The domain-averaged topographic form stress is dominated by the contribution from large scale topography, e.g., topography of scales comparable with the forcing scale. This is due to the red character of the streamfunction spectrum, and also to the anticorrelation of vorticity and topography at small scales which prevent the latter from contributing to the stress. Although the topographic small scales (in the present case, wavelengths smaller than 500 km) do not contribute to the total stress, they do have an indirect effect on the transport by affecting the dynamics of the large scales.

Although the present model is highly idealized, we hope that some of the results will prove relevant to the Antarctic Circumpolar Current. The anticorrelation of the Reynolds stress and topographic form stress, for example, is expected to persist in more complicated models, and it has been observed in a quasi-geostrophic model of the ACC with a realistic representation of the Macquarie ridge and Campbell Plateau (Wolff and Ol-

bers, personal communication). Olbers and Wenzel (1989) have recenlty analyzed the ACC circulation by inverse methods. They find the transport to be reversed (westward) at depth, as happened in some of our simulations. Their results confirm the strong influence of topography on the flow and the existence of a large vertical transfer of energy and momentum probably due to mesoscale eddies, which are the basic hypotheses underlying the present study.

*Acknowledgments.* We thank Jörg Wolff and Lien Hua for useful comments on this manuscript. The National Center for Atmospheric Research is sponsored by the National Science Foundation.

## APPENDIX

### Energy Budget for the Zonally Averaged Flow

In the equations for the energy budget, the streamfunction is decomposed into a mean ( ) and an eddy (′) part, as well as a zonal average (⟨ ⟩) and the deviation from the zonal averaged (noted by an asterisk). Therefore,

$$\psi(x, y, t) = \langle\bar{\psi}\rangle(y) + \overline{\psi_*}(x, y) + \langle\psi'\rangle(y, t) + \psi'_*(x, y, t).$$

With this decomposition of the streamfunction, the vertical energy exchanges remain similar to their usual form in Holland (1978) energy budgets. Those terms are the exchange between kinetic and potential energy, and between kinetic energy of adjacent layers. They cannot transfer energy between steady and eddy flow, or likewise between zonal mean and deviation. For example, the usual $K'_k \to P'_{k+1/2}$ term is decomposed in:

$$\langle K'_k\rangle \to \langle P'_{k+1/2}\rangle = \iint \overline{\langle\delta\psi'_{k+1/2}\rangle\langle w'_{k+1/2}\rangle}\,dxdy$$

$$K'_{*k} \to P'_{*k+1/2} = \iint \overline{\delta\psi'_{*k+1/2}w'_{*k+1/2}}\,dxdy$$

where $\delta\psi_{k+1/2}$ is the difference $(\psi_k - \psi_{k+1})$, and $w_{k+1/2}$ is the vertical velocity at interface $k + 1/2$:

$$w_{k+1/2} = \frac{f_0}{g'_{k+1/2}}\left(J(\delta\psi_{k+1/2}, \psi_{k+1/2}) - \frac{\partial}{\partial t}\delta\psi_{k+1/2}\right),$$

with $\psi_{k+1/2}$ defined as

$$\psi_{k+1/2} = \frac{H_{k+1}}{H_k + H_{k+1}}\psi_k + \frac{H_k}{H_k + H_{k+1}}\psi_{k+1}.$$

Lateral and bottom friction terms, as well as forcing terms, are also straightforward.

Another example is the transfer of steady energy between layer $k$ and layer $k + 1$, which is decomposed as

$$\langle\bar{K}_k\rangle \to \langle\bar{K}_{k+1}\rangle = \iint \langle\bar{\psi}_{k+1/2}\rangle\bar{w}_{k+1/2}\,dxdy$$

$$\bar{K}_{*k} \to \bar{K}_{*k+1} = \iint \bar{\psi}_{*k+1/2}\bar{w}_{k+1/2}\,dxdy.$$

The expression for $w$ being nonlinear, $\bar{w}$ contains a term due to the standing eddies $\bar{w}^s$ and a term due to the time average of the transients. Let us consider the former contribution:

$$\iint (\langle\bar{\psi}_{k+1/2}\rangle + \bar{\psi}_{*k+1/2})\bar{w}^s_{k+1/2}\,dxdy = \iint \frac{f_0}{g'_{k+1/2}}\bar{\psi}_{k+1/2}J(\bar{\psi}_k, \bar{\psi}_{k+1})\,dxdy = 0.$$

The total downward transfer of mean energy due to the standing eddies is zero when integrated over a closed or periodic domain. Therefore, if standing eddies transfer zonal mean energy downward, this must be compensated by an upward transfer of nonzonal mean energy. There is not such a constraint on the transients, which can perform the necessary domain-averaged downward transfer of time-mean energy.

There are new terms in the energy balance describing energy transfers between the zonal mean and the standing eddies. The six kinetic energy transfer terms for layer $k$ are:

$$\langle K'_k\rangle \to \langle\overline{K_k}\rangle = 0$$

$$K'_{*k} \to \overline{K_{*k}} = \iint \overline{\psi_{*k}J(\psi'_{*k}, \nabla^2(\psi'_{*k} + \langle\psi'_k\rangle))}\,dxdy$$

$$\langle K'_k\rangle \to K'_{*k} = \iint \overline{\psi'_{*k}J(\langle\psi'_k\rangle, \nabla^2(\psi'_{*k} + \overline{\psi_{*k}}))}\,dxdy$$

$$\langle\overline{K_k}\rangle \to K'_{*k} = \iint \overline{\psi'_{*k}J(\langle\overline{\psi_k}\rangle, \nabla^2\psi'_{*k})}\,dxdy$$

$$\langle K'_k\rangle \to \overline{K_{*k}} = \iint \overline{\psi_{*k}J(\langle\psi'_k\rangle, \nabla^2\psi'_{*k})}\,dxdy$$

$$\langle\overline{K_k}\rangle \to \overline{K_{*k}} = \iint \overline{\psi_{*k}}J(\langle\overline{\psi_k}\rangle, \nabla^2\overline{\psi_{*k}})\,dxdy.$$

The first term is zero since the jacobian of a purely zonal flow vanishes.

Potential energy transfer terms are similar, with $\psi_k$ replaced by $\delta\psi_{k+1/2}$ and the relative vorticity $\nabla^2\psi_k$ replaced by $\psi_{k+1/2}$.

The topographic transfer term exists only in the bottom layer $k = n$.

$$TK'(\langle K' \rangle \to K'_*) = -\iint \overline{\frac{\partial \langle \psi' \rangle}{\partial y} \frac{\partial h}{\partial x} \psi'_*} dxdy$$

$$\overline{TK}(\langle \bar{K} \rangle \to \overline{K_*}) = -\iint \frac{\partial \langle \bar{\psi} \rangle}{\partial y} \frac{\partial h}{\partial x} \overline{\psi_*} dxdy.$$

The steady topographic energy transfer $\overline{TK}$ is the product of the zonally averaged steady vlocity $\langle \bar{u} \rangle(y)$ with the usual topographic drag $\bar{T}(y)$ which appears in the momentum equation. The transient transfer $TK'$ has no analogy in the time-averaged momentum equation.

## REFERENCES


Bretherton, F. P., and D. B. Haidvogel, 1976: Two dimensional turbulence above topography. *J. Fluid Mech.*, **78**, 129–154.

Charney, J. G., and J. D. de Vore, 1979: Multiple flow equilibria in the atmosphere and blocking, *J. Atmos. Sci.*, **36**, 1205–1216.

——, and D. M. Straus, 1980: Form-drag instability, multiple equilibria and propagating planetary waves in a baroclinic, orographically forced, planetary wave system. *J. Atmos. Sci.*, **37**, 1157–1176.

Gill, A. E., and K. Bryan, 1971: Effects of geometry on the circulation of a three-dimensional southern-hemisphere ocean model. *Deep-Sea Res.*, **18**, 685–721.

Herring, J. R., 1977: On the statistical theory of two dimensional topographic turbulence, *J. Atmos. Sci.*, **34**, 1731–1750.

Holland, W. R., 1978: The Role of Mesoscale eddies in the General Circulation of the Ocean-Numerical experiments using a wind-driven quasi-geostrophic model. *J. Phys. Oceanogr.*, **8**, 363–392.

Holloway, G., 1978: A spectral theory of non linear barotropic motion above irregular topography, *J. Phys. Oceanogr.*, **8**, 414–427.

——, 1987: Systematic forcing of large-scale geophysical flows by eddy-topography interaction. *J. Fluid Mech.*, **184**, 463–476.

Johnson, G. C., and H. Bryden, 1989: On the size of the Antarctic Circumpolar current. *Deep-Sea Res.*, **36**, 39–53.

McWilliams, J. C., 1977: A note on a consistent quasi-geostrophic model in a multiply connected domain. *Dyn. Atmos. Oceans*, **1**, 427–441.

——, and J. Chow, 1981: Equilibrium turbulence I: a reference solution in a $\beta$-plane channel. *J. Phys. Oceanogr.*, **11**, 921–949.

——, W. R. Holland and J. Chow, 1978: A description of numerical Antarctic circumpolar currents. *Dyn. Atmos. Oceans*, **2**, 213–291.

Munk, W. H., and E. Palmen, 1951: Note on the dynamics of the Antarctic Circumpolar current, *Tellus*, **3**, 53–55.

Nowlin, W. D., and J. M. Klinck, 1986: The physics of the Antarctic Circumpolar current, *Rev. Geophys.*, **24**, 469–491.

Rhines, P. B., 1970: Edge-, bottom-, and Rossby waves in a rotating stratified fluid. *Geophys. Fluid. Dyn.*, **1**, 273–302.

——, 1977: The dynamics of unsteady currents. Marine Modelling, The Sea, Vol. 6, E. D. Goldberg, I. N. McCane, J. J. O'Brien and J. H. Steele, Eds., Wiley, 189–318.

Salmon, R., G. Holloway and M. C. Henderschott, 1976: The equilibrium statistical mechanics of simple quasi-geostrophic models. *J. Fluid Mech.*, **75**, 691–703.

Treguier, A. M., 1989: Topographically generated steady currents in barotropic turbulence. *Geophys. Astrophys. Fluid. Dyn.*, **47**, 43–68.

——, and B. L. Hua, 1988: Influence of bottom topography on quasi-geostrophic turbulence in the ocean. *Geophys. Astrophys. Fluid. Dyn.*, **43**, 265–305.

Wolff, J. O., and D. J. Olbers, 1989: The dynamical balance of the Antarctic Circumpolar Current studied with an eddy-resolving quasigeostrophic model. *Mesoscale/Synoptic Coherent Structures in Geophysical Turbulence*, J. C. J. Nihoul, Ed., Elsevier Oceanogr. Ser. 50, 435–458.